Dynamic interpretation of maternal inputs by the *Drosophila* segmentation gene network

Feng Liu, Alexander H. Morrison, and Thomas Gregor[1]

Joseph–Henry Laboratories of Physics and the Lewis–Sigler Institute for Integrative Genomics, Princeton University, Princeton, NJ 08544

Edited by Eric D. Siggia, The Rockefeller University, New York, NY, and approved March 12, 2013 (received for review November 30, 2012)

Patterning of body parts in multicellular organisms relies on the interpretation of transcription factor (TF) concentrations by genetic networks. To determine the extent by which absolute TF concentration dictates gene expression and morphogenesis programs that ultimately lead to patterns in *Drosophila* embryos, we manipulate maternally supplied patterning determinants and measure readout concentration at the position of various developmental markers. When we increase the overall amount of the maternal TF Bicoid (Bcd) fivefold, Bcd concentrations in cells at positions of the cephalic furrow, an early morphological marker, differ by a factor of 2. This finding apparently contradicts the traditional threshold-dependent readout model, which predicts that the Bcd concentrations at these positions should be identical. In contrast, Bcd concentration at target gene expression boundaries is nearly unchanged early in development but adjusts dynamically toward the same twofold change as development progresses. Thus, the *Drosophila* segmentation gene network responds faithfully to Bcd concentration during early development, in agreement with the threshold model, but subsequently partially adapts in response to altered Bcd dosage, driving segmentation patterns toward their WT positions. This dynamic response requires other maternal regulators, such as Torso and Nanos, suggesting that integration of maternal input information is not achieved through molecular interactions at the time of readout but through the subsequent collective interplay of the network.

gap genes | gene regulatory networks | pattern formation

The macroscopic patterns of multicellular organisms are established by the molecular interplay within transcription factor (TF) networks that give rise to corresponding patterns of gene expression during the earliest stages of embryonic development (1). During these stages, individual cells acquire information about their position within the embryo by interpreting multiple TF concentration gradients and other factors that are inhomogeneously distributed in the egg (2–5). However, the quantitative and dynamic nature of this interpretation and the subsequent response of the network are not well understood. Specifically, little is known about the ability of individual DNA loci to measure TF concentrations precisely or how these loci integrate information from measurements of multiple input concentrations. One can distinguish between two broad classes of system-level viewpoints of how this information is interpreted by the network. In one view, information-rich maternal gradients provide all the spatial cues for the final patterns and the information is relayed in a step-by-step feed-forward manner, consistent with the traditional threshold-dependent readout model (6). In the other view, maternal gradients provide the initial spatial cues to downstream genes that then cross-regulate in an otherwise self-organized network (7–16).

The *Drosophila* embryo provides an excellent system in which these problems can be addressed in a physiologically relevant context and the influences from different input factors can be disentangled (4, 5, 17). Soon after the egg is activated, naturally varying protein gradients establish in the developing egg, which are interpreted by zygotic genes in a concentration-dependent manner. One such gradient is the anterior determinant Bicoid (Bcd) (18, 19), whose mRNA is maternally deposited at the anterior pole of the egg (20, 21). Bcd acts as a TF and activates target genes, such as the gap gene *hunchback* (*hb*) and the primary pair-rule gene *even-skipped* (*eve*) (22, 23). This cascade of regulatory events generates spatial patterns that are precise enough to distinguish neighboring nuclei based on their levels of gene expression (24), and these patterns are reproducible from embryo to embryo (25–28).

If Bcd concentration directly controls cell fate as predicted by the traditional threshold-dependent readout model (6), the Bcd-dependent patterning markers must always form at the same absolute Bcd concentration, even in genetic backgrounds of altered *bcd* copy numbers of variable strengths (18, 22, 29) (Fig. S1). The cephalic furrow (CF), a morphological feature that separates the head and thoracic region of the early embryo, has provided a useful test for this idea. In embryos with altered *bcd* copy numbers, the CF's location along the anterior-posterior (AP) axis shifts with respect to WT, but likely not in a strict concentration-dependent manner (18, 25, 30). However, to test how Bcd is interpreted quantitatively, it is necessary to measure actual Bcd protein concentration instead of relying on the bcd copy number. The expression of *bcd* could be negatively regulated, and expression levels could vary for exogenous *bcd* alleles, because transgenes insert randomly in the genome and their expression levels depend on the chromosomal insertion site (31).

To address the above, we generated an allelic series of transgenic fly strains with various absolute Bcd concentrations, exploiting the chromosome position effect (31). Performing precise measurements on embryos of these fly strains, we quantified the expression levels of the various transgenes. We found that multiple insertions in the same embryo add their individual strengths in an entirely linear manner over a fivefold range in Bcd concentration, suggesting no feedback is involved in Bcd expression. When we measure the network's reaction to fivefold absolute Bcd concentration changes, we observe that the network responds nearly perfectly to Bcd at early developmental stages but subsequently adapts to the dosage alteration, partially restoring the shifted AP patterns to their WT positions. Interestingly, this dynamic process vanishes when these measurements are repeated in flies mutant for other maternal inputs, such as *torso* (*tor*) or *nanos* (*nos*). These findings suggest that the dynamic response is a result of interacting inputs and that the system achieves integration of positional information from various inputs not by molecular interactions at a specific enhancer when Bcd is turning on genes but through the subsequent downstream interplay of the network.

Author contributions: F.L. and T.G. designed research; F.L., A.H.M., and T.G. performed research; F.L., A.H.M., and T.G. analyzed data; and F.L. and T.G. wrote the paper.

The authors declare no conflict of interest.

This article is a PNAS Direct Submission.

Data deposition: The data reported in this paper have been deposited in the Dryad repository, http://dx.doi.org/ (accession no. 10.5061/dryad.2j9p4).

[1]To whom correspondence should be addressed. E-mail: tg2@princeton.edu.

This article contains supporting information online at www.pnas.org/lookup/suppl/doi:10.1073/pnas.1220912110/-/DCSupplemental.

Results

Generation of 20 Fly Lines with 5.7-Fold Bcd Concentration Changes. To vary Bcd concentrations, we first generated six *Drosophila* fly lines to use as founder lines, in which endogenous Bcd is replaced by the bcd^{E1} null phenotype and Bcd activity was supplied by a transgene producing a fully functional fluorescent EGFP-Bcd fusion protein (called Bcd-GFP hereafter). We performed live imaging to measure absolute Bcd concentrations and compared nuclear Bcd-GFP gradients across these fly lines. Nuclear Bcd-GFP concentration gradients were extracted from individual embryos in coronal optical sections (Fig. 1 *A* and *B*) using a custom-built two-photon microscope with significantly improved signal-to-noise ratios compared with previous measurements (*SI Materials and Methods*). The gradient reproducibility is ∼15% across almost the entire AP axis, except for the most anterior and posterior ends (Fig. 1*C*). Statistically, the accuracy with which we can distinguish between Bcd dosages of two fly lines is set by our measurement noise and by the intrinsic reproducibility of Bcd concentrations in a population of embryos, which we determined at 14.5% by the dosage fluctuations within a single fly line (Fig. 1*D*); thus, the discrimination accuracy in a typical imaging session with a sample size of ∼10 embryos approaches $0.145/\sqrt{10} \sim 4\%$. The final Bcd dosage of a typical fly line was measured by comparing its average Bcd-GFP gradient with a concurrently imaged average Bcd-GFP gradient of a reference fly line named $2X_A$ (Fig. 1*E* and *SI Materials and Methods*), whose Bcd concentration is close to the endogenous WT Bcd concentration (see below). The Bcd dosages of the six founder lines range from 0.77 to 1.09, with an average measurement error of 7 ± 2% (Fig. 1*E*, *Inset*).

Using these 6 founder lines, we generated a series of 20 Bcd-GFP expressing fly lines by genetic combination (Fig. 1*F* and Table S1). The copy numbers of *egfp-bcd* transgene insertions

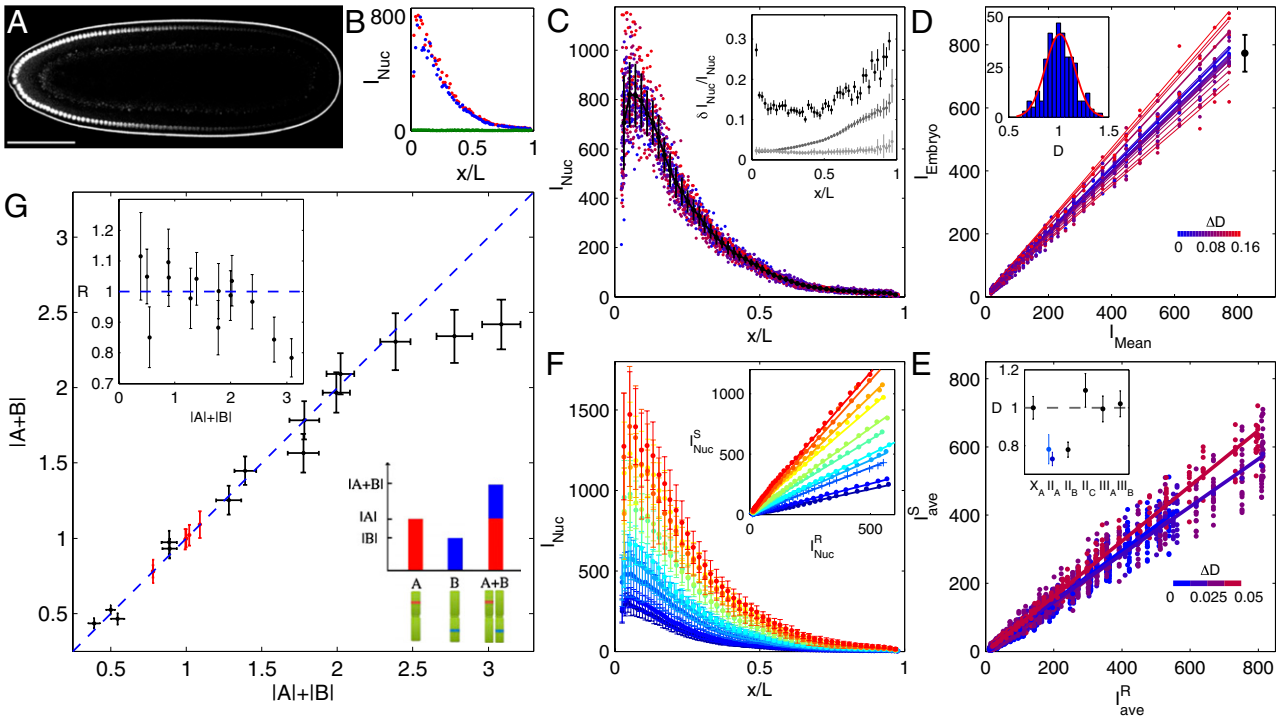

Fig. 1. Absolute Bcd-GFP concentration and dosage measurements. (*A*) Scanning two-photon microscopic image of a *Drosophila* embryo (dorsal view of midcoronal plane) expressing a Bcd-GFP fusion protein (reference fly line $2X_A$; described in the main text). (Scale bar: 100 μm.) (*B*) Apparent Bcd-GFP nuclear intensity, I_{Nuc}, in each visible nucleus in *A* plotted vs. AP position *x* in units of egg length *L*; the left and right sides of the AP axis are shown in red and blue, respectively (∼70 nuclei each). The background (green) is measured in 12 WT embryos (same imaging conditions). (*C*) Nuclear Bcd-GFP intensities of $2X_A$ embryos measured in a single imaging session (different colors for 21 individual embryos); means and SDs of nuclei in 50 equidistant bins are shown in black. (*C*, *Inset*) For each bin, the SD, δI_{Nuc}, divided by the mean I_{Nuc} is shown as a function of fractional embryo length *x/L* (dark points); error bars are determined from bootstrapping. Dark and light gray curves show imaging noise and image processing error, respectively. (*D*) Scatter plots (dots) and linear fits (lines) of embryo intensity, I_{Embryo} (I_{Nuc} of each of the 21 binned Bcd-GFP gradients in *C*) vs. mean intensity, I_{Mean} [average binned Bcd-GFP gradient (black curve in *C*)]. The slope of each linear fit defines the dosage *D* of an individual embryo, relative to the average Bcd dosage of the given fly line. Color encodes fractional change from mean dosage $D = 1$ (color bar). The black error bar represents dosage spread in this particular imaging session ($\sigma = 8\%$). (*D*, *Inset*) Histogram of 360 single-embryo dosages ($2X_A$ embryos, 33 imaging sessions). The red line is a Gaussian fit with an SD of 14.5%. (*E*) Dosage measurement of sample fly line $2II_A$. Different colors correspond to four independent imaging sessions. Dots are I^S_{ave}(binned means of nuclear Bcd-GFP concentrations of individual embryos) plotted against I^R_{ave} (average binned mean nuclear Bcd-GFP concentration of the reference fly line $2X_A$) measured side by side in the same imaging session. The dosage extracted per imaging session from the slope of a linear fit (solid lines) is $D = \{0.73, 0.71, 0.70, 0.78\}$. Color encodes the fractional change from the mean dosage $D = 0.73 \pm 0.03$ for the four sessions (color bar), implying a dosage reproducibility of ∼4%. (*E*, *Inset*) Average dosage for 6 homozygous fly lines with respect to dosage $D = 1$ (dashed line). Black data points correspond to a single fit to the combined data of all imaging sessions; error bars are determined from bootstrapping. For fly line $2II_A$, a linear fit to data from pooled imaging sessions (light blue) and the average of linear fits to individual imaging sessions (dark blue) are shown. (*F*) Average binned Bcd-GFP gradients of 11 fly lines with Bcd-GFP dosages as indicated in Table S1; error bars are across all nuclei of all embryos in a given bin. (*F*, *Inset*) Linear fits to scatter plots of average Bcd-GFP gradients of the sample fly lines compared with the average Bcd-GFP gradients of the reference fly line $2X_A$. The "+" symbol depicts average of data in *E*. (*G*) Scatter plot of measured Bcd-GFP dosage $|A+B|$ of fly line $A + B$ and the expected Bcd-GFP dosage $|A| + |B|$ from individual measurements of fly lines *A* and *B*. The means and SDs of the measured Bcd-GFP dosage of the 6 founder lines and the 14 genetically constructed fly lines are shown in red and black, respectively. Vertical error bars correspond to uncertainty in dosage determination. Horizontal error bars are obtained from error propagation (*SI Materials and Methods*). The blue dashed line shows $|A+B| = |A| + |B|$. (*G*, *Inset*) Deviation from 1 of the ratio $R = |A+B|/(|A| + |B|)$ is less than 20% for all fly lines.

range from one to six, and Bcd dosages relative to WT span a range of 0.44–2.4, which is well within the linear range of our imaging setup (Fig. S2). Taking advantage of the small dosage differences between the founder lines, the relative increment of the Bcd dosage is comparable to the variability of the Bcd concentration within individual fly lines (Fig. 1*D*), allowing us to tune Bcd dosage systematically over an almost sixfold range with very fine (<10%) discrete steps. As a result, we have created an effective tunable parameter of input concentration that changes in precise and discrete quantities, comparable to the well-known inducible systems in yeast or bacteria (32). Note that as the absolute Bcd concentration changes across fly lines, neither the shape nor the reproducibility of the gradients changes significantly (Fig. S3). However, in our live Bcd-GFP measurements, the delayed EGFP maturation alters the shape of the Bcd gradient slightly, increasing the mean length constant by ∼15% (*SI Materials and Methods* and Fig. S4).

Multiple *bcd* Alleles Operate Perfectly Linearly. To check whether there is a range around the WT dosage where dosage perturbations are linear and whether individual alleles operate independently, we tested our genetically constructed fly lines arithmetically. We evaluated whether the sum of two fly lines A and B with dosages $|A|$ and $|B|$ is identical to the dosage $|A + B|$ measured in the fly line $A + B$ that is the genetic composition of the two individual lines (cartoon in Fig. 1*G*). Surprisingly, for the 14 combined fly lines we tested, all data points within the dosage range of 0.44 and 2.3 fall within error bars on the blue dashed line of $|A + B| = |A| + |B|$, and the ratio of measured to expected dosages is within 20% of unity (Fig. 1*G*). Thus, the amount of Bcd produced in the combined fly line $A + B$ is the exact summed amount of Bcd produced from the individual fly lines A and B. Only for the two largest dosages that we constructed, 2.34- and 2.4-fold the reference dosage, did we observe a deviation from the diagonal, with predicted dosages of 2.8 and 3.1, respectively. These measurements demonstrate a fivefold physiological dosage range in which Bcd concentrations can be linearly manipulated, allowing us to probe the network's response to absolute input concentration in a quantitative, systematic manner.

These results indicate that Bcd expression levels are set by a simple linear feed-forward mechanism, and that the amount of Bcd protein produced from each *bcd* allele in the genome is independent of any of the other *bcd* alleles present in the same genome. This suggests that the extraordinary reproducibility of the Bcd gradients observed above and in previous work (28) is unlikely to involve any feedback regulation on Bcd expression. We can essentially exclude mechanisms involving Bcd autoregulation that could lead to the precise control of (*i*) the number of *bcd* mRNA deposited during oogenesis or (*ii*) the number of Bcd protein molecules produced during the early stages in the zygote. It further means that in the identified linear range, the system must be devoid of any adjustment scheme that would shift dosage levels back to a WT set point. No limiting factor is present in the system, which would lead to a saturated operation level in setting up the Bcd source, and hence would not be able to cope with too much or too little Bcd in the system.

Quantitative Measurements of CF Shifts on Absolute Bcd Concentration Changes. Classically, the most straightforward way to assess the effect of *bcd* copy numbers on the downstream gene regulatory network is to quantify the location of the CF (18, 33). Here, we follow this traditional approach but ask whether the absolute Bcd concentration in cells of the forming CF is unchanged in fly lines with different overall Bcd dosage. The CF appears at the onset of gastrulation as a change in shape and apical positioning of a single row of cells. Genetically, the position of the invaginating cells is defined by the overlapping expression of two Bcd targets: the head gap gene *buttonhead* and *eve* (34). This position

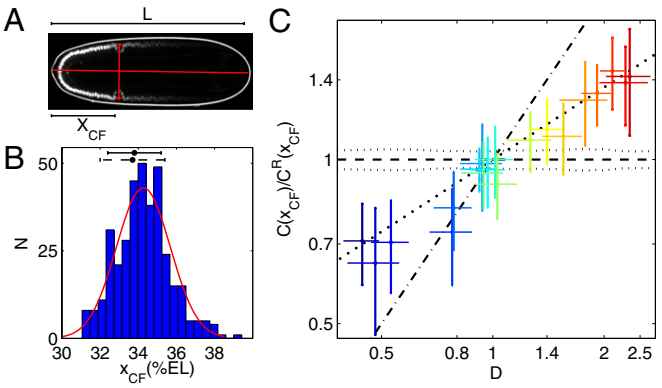

Fig. 2. CF position measurements and response to Bcd dosage perturbations. (*A*) Scanning two-photon microscopic image of the same *Drosophila* embryo as in Fig. 1*A*, ∼1 h later in its development. The CF position is defined relative to embryo length L as $x_{CF} = X_{CF}/L$, where X_{CF} is the distance from the anterior pole to the intersection between the AP axis and the line connecting left and right CF invaginations (red dots, manually selected). (*B*) Histogram of x_{CF} of 364 $2X_A$ embryos. The red line is a Gaussian curve plotted with the corresponding distribution mean (34.3%EL) and SD (1.2%EL). The CF positions measured by bright-field microscopy (dorsal view) for $2X_A$ (dark dashed error bar) and WT embryos (dark error bar) are 33.7 ± 1.7%EL and 33.8 ± 1.4%EL, respectively. Experimental measurement errors (0.3–0.6% EL) are illustrated in Fig. S5. (*C*) Log-log plot of the relative Bcd-GFP concentration at CF positions, $C(x_{CF})/C^R(x_{CF})$, as a function of Bcd dosage D for 20 fly lines. $C(x_{CF})$ and $C^R(x_{CF})$ are Bcd-GFP concentrations at the CF position of the sample fly line and the reference fly line $2X_A$, respectively. Error bars are SDs of relative $C(x_{CF})$ (vertical) and D (horizontal). Different colors represent different fly lines. The slope of the linear fit (bold dotted line) to 1,187 single embryo data points is $S_c = 44 \pm 2\%$ ($R^2 = 0.74$). Dashed and dotted lines, respectively, show the expected means and SDs of relative $C(x_{CF})$ in a scenario in which $C(x_{CF})$ is unchanged in the different dosage backgrounds. The dash-dotted line shows the expected relative $C(x_{CF})$ if CF location is independent of Bcd dosage.

can be easily determined either directly by bright-field microscopy or, as in our case, by residual Bcd-GFP that remains in anterior nuclei during gastrulation (Fig. 2*A*). Thus, conveniently, Bcd gradients and CF positions can be measured in the same embryo, developmentally separated by ∼50 min.

To measure the location of the CF (x_{CF}) reliably, great control has to be exerted on embryo orientation and on the exact timing of the measurement (*SI Materials and Methods* and Fig. S5). Systematic errors are minimized when embryos are imaged from a dorsal view in the coronal plane (Fig. 2*A*). Under these conditions, we obtained a value of $x_{CF} = 34.3 \pm 1.2\%$ embryo length (EL) for our reference fly line $2X_A$ (Fig. 2*B*), which is nearly identical to the WT (Oregon-R) CF position of 33.8 ± 1.4%EL, measured via bright-field microscopy (Fig. 2*B*). The latter agreement justifies our assessment that the Bcd dosage in fly line $2X_A$ is very close to the endogenous WT Bcd dosage.

A direct test of whether changing the Bcd concentration is equivalent to changing the position is to test whether the Bcd concentration at x_{CF}, $C(x_{CF})$, remains constant on changes in Bcd dosage D in the different fly lines. Fig. 2*C* shows a log-log plot of the measured maturation-corrected mean and SD of relative C (x_{CF}) as a function of D for 20 fly lines (*SI Materials and Methods* and Fig. S6*A*). We detect a quasilinear relationship with a slope $S_C = 44 \pm 2\%$ that deviates significantly from zero, the value predicted for the unchanged concentration readout. The magnitude of S_C expresses the deviation of $C(x_{CF})$ of a sample fly line with a particular overall Bcd dosage from the expected $C(x_{CF})$ as measured in the reference fly line $2X_A$. Thus, over the fivefold change in D, we measure only a twofold change in the response, suggesting that the network adapts, but not perfectly. This means that shifts in the position of the CF are reduced compared with predicted values from the unchanged concentration readout

(Fig. S6*B*), confirming previous qualitative observations (18, 25). Overall, these results indicate that the naive assumption that changes in position and in concentration space are equivalent holds only to within a factor of 2. However, it remains unclear whether this discrepancy is informative about the general functioning of the system.

Segmentation Network Responds Dynamically to Bcd Dosage Alterations. The CF is a positional marker that is regulated by the segmentation gene network and only generated at the end of the maternal/gap/pair-rule gene cascade. This raises the question of whether we also observe a relationship for the earlier underlying gene expression patterns similar to the one we discovered between Bcd concentrations in CF-forming cells and the overall Bcd dosage. If the fate and position of the CF reflect the initial reading of the Bcd gradient, we also expect to see the same twofold change in Bcd concentration at the early patterning boundaries of the gap and pair-rule genes. On the other hand, if the initial response is perfectly concentration-dependent, we expect to see Bcd concentrations at these positions to vary only within 0.1-fold (or 10%; i.e., the limit set by the precision of our measurements).

To address this question, we measured the effective input-output relationships between Bcd and the gap genes in fly lines with differing Bcd-GFP dosages. Fig. 3 *A*–*D* shows representative input-output functions for the gap genes Hb and Giant (Gt) for early and late time points in nuclear cycle (n.c.) 14. Interestingly, the functions evolve with time. At early stages, they generally tend to overlap and are independent of overall Bcd dosage. At later stages, the gaps between the different dosage curves widen, suggesting an overall dynamic response of the gap gene network. Dynamic gap gene expression patterns have been reported previously (9, 13, 16, 35); the dynamic we observe here, however, is specific in that it is a response to altered overall input dosage.

We can make this observation more quantitative by measuring Bcd concentration at the location of the posterior boundary of the anterior Hb pattern, $C(x_{Hb})$, for the different Bcd dosages (*SI Materials and Methods* and Figs. S7 and S8). Early during n.c. 14, regardless of the dosage background, $C(x_{Hb})$ is very close to the Bcd concentration of cells at x_{Hb} in a WT background (Fig. 3*E*), as expected within a threshold-dependent readout model (6). However, as development progresses, relative $C(x_{Hb})$ continually changes toward the relative Bcd concentrations in cells of forming CFs, as portrayed in Fig. 2*C* and shown by the dotted lines in Fig. 3 *E* and *F*. This change demonstrates a dynamic response of the Hb profile to altered Bcd input dosages. On a fourfold Bcd dosage change, the change of $C(x_{Hb})$ is only 0.3-fold (or 30%) early in n.c. 14, and it keeps increasing to reach a 1.6-fold change later in n.c. 14. Consequently, in altered Bcd dosage backgrounds, the Hb pattern boundaries are continuously driven toward their WT locations by a dynamic process (Fig. S7*D*). We notice that originally anteriorly shifted boundaries for $D < 1$ migrate posteriorly and originally posteriorly shifted boundaries for $D > 1$ migrate anteriorly. The more the Bcd dosage is altered, the more relative shifts occur as development progresses.

Fig. 3*F* summarizes the changes in Bcd concentrations at particular positions of several representative segmentation markers, including Hb, Gt, Krüppel (Kr), and Eve (the equivalent plot for the CF position is shown in Fig. 2*C*). For early Gt and Kr profiles, fourfold dosage changes leave Bcd concentrations at the respective boundaries nearly unchanged (within 27% and 23%, respectively). In later stage n.c. 14 embryos, Bcd concentrations at the gap gene boundaries have changed by as much as those of CF-forming cells, as can be seen by the similarity in their respective slopes. We see a similar dynamic evolution for the effective Bcd concentration readout of cells defining stripe 1 of the Eve pattern (Eve–Stripe-1), which, as expected, coincides with the CF at late n.c. 14 stages (Fig. 3*F*).

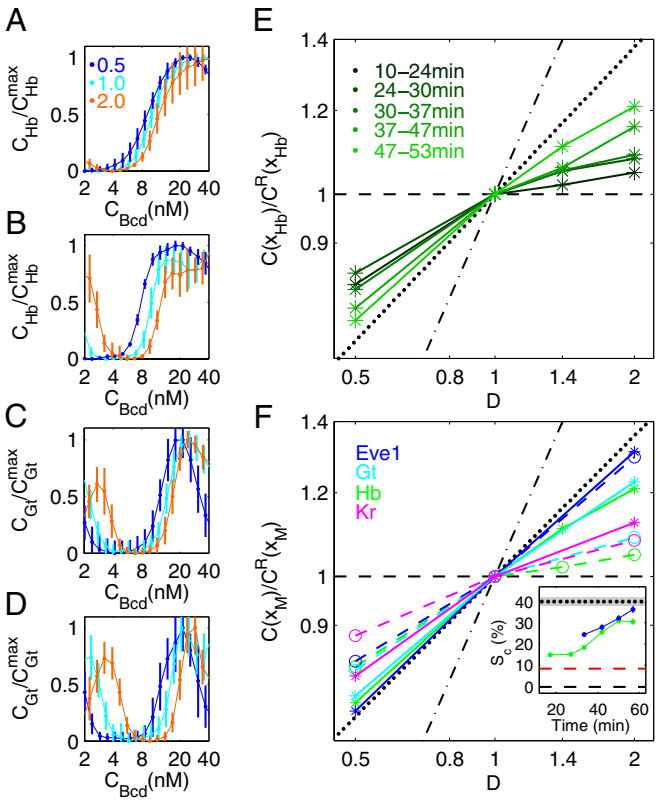

Fig. 3. Dynamic network response to Bcd dosage alterations. Average input-output relations of gap genes *hb* (*A* and *B*) and *gt* (*C* and *D*) as a function of input Bcd concentration for three Bcd dosages *D*: 0.5 (blue), 1.0 (cyan), and 2.0 (orange). Hb and Gt concentrations (C_{Hb} and C_{Gt}) are extracted from immunofluorescence profiles of fixed embryos, staged using the invagination depth of the membrane furrow (35), and normalized by the respective maximum concentrations, C^{max}_{Hb} and C^{max}_{Gt}. Profiles are shown for n.c. 14 stages at 8–24 min (*A* and *C*) and at 47–53 min (*B* and *D*). Error bars are SDs in bins of size 3%EL. (*E*) Log-log plot of relative Bcd-GFP concentration at the Hb boundary, $C(x_{Hb})/C^R(x_{Hb})$, as a function *D*. Embryos are separated into five time classes (10–24 min, 24–30 min, 30–57 min, 37–47 min, and 47–53 min) into n.c. 14, shown as shades of green. Black lines are as in Fig. 2C. (*F*) Log-log plot of relative Bcd-GFP concentrations at four representative segmentation marker positions as a function of Bcd dosage *D*, including the most anterior peak of the expression pattern of Eve (blue), the posterior boundaries of anterior patterns of Gt (cyan) and Hb (green), and the posterior boundary of Kr (magenta). The dashed and solid colored lines are for early (12 ± 7 min; Eve at 34 ± 3 min) and late (50 ± 3 min) n.c. 14, respectively. Black lines are as in *E*. (*F*, *Inset*) Time dependence of the slope S_c for x_{Hb} (green) and x_{Eve1} (blue) (extracted from Fig. S6*D*; *SI Materials and Methods*). For comparison, the black dotted line (gray zone) is the average (SD) of the final slope for the CF (linear fit in Fig. 2*C* and Fig. S6*B*; *SI Materials and Methods*). The red dashed line shows S_c for the CF of maternal mutant fly lines (Fig. S6*C*). The black dashed line is expectation from the threshold-dependent readout model.

Maternal Factors Contribute to Dynamic Adjustments. To uncover the mechanism underlying the observed dynamic adjustments of the segmentation gene network on Bcd dosage changes, we measured the network response in genetic backgrounds of null mutations for the maternal genes *torso-like* (*tsl*) and/or *nos*, which provides positional information independent of Bcd. Because *tsl* is required to trigger the activation of Tor receptor tyrosine kinase, disabling *tsl* blocks Tor function. Although Bcd, Nos, and Tor belong to anterior, posterior, and terminal maternal

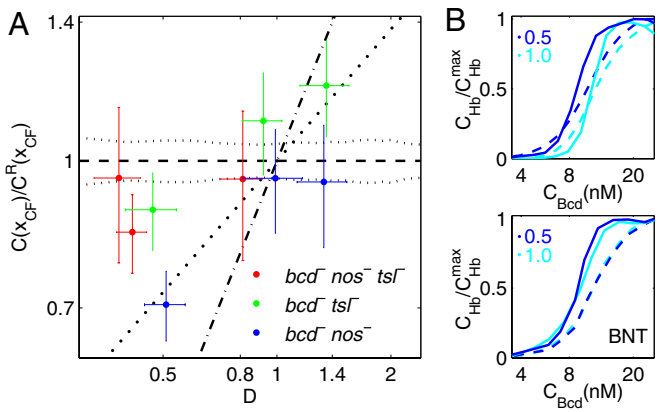

Fig. 4. Network response to Bcd dosage alterations in maternal mutant backgrounds. (*A*) Log-log plot of the relative $C(x_{CF})$ vs. Bcd dosage D for fly lines carrying various copies of the Bcd-GFP transgene in maternal mutant backgrounds. Red, green, and blue data points represent means and SDs of $C(x_{CF})$ normalized by $C^R(x_{CF})$ of the reference fly line $2X_A$ (vertical error bar) and Bcd dosage (horizontal error bar) of fly lines with the maternal mutations $bcd^{E1}nos^{BN}tsl^{-}$, $bcd^{E1}tsl^{-}$, and $bcd^{E1}nos^{BN}$, respectively. The black lines correspond to their identical counterparts in Fig. 2*C*, which are in a bcd^{E1} mutant background. (*B*) Comparison of the dynamic response of the Bcd-Hb input-output relations to Bcd dosage perturbations [$D = 0.5$ (blue) and $D = 1$ (cyan)] in a bcd^{E1} background (*Upper*) and in a $bcd^{E1}nos^{BN}tsl^{-}$ (BNT) mutant background (*Lower*). Hb concentration C_{Hb} is normalized by its maximum value C_{Hb}^{max}. Dashed and solid lines are Bcd-Hb input-output relations extracted from embryos at 8–24 min and at 47–53 min into n.c. 14, respectively.

coordinate systems, respectively, there are several lines of evidence that they do not work independent of each other (4, 5, 17, 36). Therefore, Tor and/or Nos could indeed contribute to the observed dynamic changes of the anterior segmentation markers.

We repeated our CF measurements in fly lines that carry a null mutation for *tsl* and/or *nos* and have Bcd dosage backgrounds ranging from 0.4- to 1.4-fold the WT dosage (Table S1). Fig. 4*A* shows Bcd concentrations at CF positions vs. Bcd dosage measurements in nine of such maternal mutant fly lines. The fly lines in a *tsl*-null background (green data points in Fig. 4*A*) have Bcd concentrations in CF-forming cells that are independent of overall dosage for $D < 1$ (i.e., they fall close to the black dotted line corresponding to WT Bcd concentrations at that particular position). Hence, the effect that we saw in WT backgrounds of altered effective Bcd concentrations has vanished. This result is confirmed in the double-null mutant for *tsl* and *nos* (red data points in Fig. 4*A*). On the other hand, disabling *nos* only is insufficient to cause the effect to disappear (blue data points in Fig. 4*A*). These results indicate that for $D < 1$, the maternal factor Tsl, but not Nos, contributes to the Bcd concentration adjustment at the CF location on Bcd dosage changes, leading to larger positional CF shifts than in the WT case (Fig. S6*C*). Therefore, *tsl* has a likely role in the observed dynamics of the segmentation gene network, and multiple maternal inputs are integrated over time to generate the final state of the system. Remarkably, we see a similar, albeit weaker, effect for $D > 1$; in this regime, however, the roles of *nos* and *tsl* seem to be inverted, which may simply indicate that for posterior boundary shifts, it is the maternal Nos gradient that influences the system more significantly than the posterior Tor gradient.

We further confirmed that the dynamic response of the segmentation network indeed vanishes when the maternal factors Tor and Nos are both nonfunctional. Fig. 4*B* shows a comparison of the effective input-output relationships between Bcd and Hb. In contrast to fly lines with WT background, the fly lines carrying double-null mutations for both *tsl* and *nos* have overlapping effective input-output functions under different Bcd dosage backgrounds at both early and late developmental stages. Together, these data suggest that the observed dynamic changes in concentration interpretation are the result of multiple inputs.

Discussion

One potential origin of the observed dynamic adjustment lies in a dynamic integration of maternally provided positional information by the segmentation gene network (10, 37, 38). At early developmental stages, initial gap gene expression boundaries are solely determined by maternal factors. The posterior boundaries of Hb and Gt are determined by the activation of Bcd, whereas the anterior boundaries of Knirps (Kni) and Kr are determined by the repression of maternal Hb, which is regulated by Nos (39). As development progresses, however, accumulated gap gene products engage in cross-regulation (39) and mediate the integration of positional information of multiple independent maternal factors at the various boundary interfaces. This mechanism could restrict shifts of one boundary resulting from a particular maternal factor by the opposing boundary. Hence, the observed dynamic adjustment could function as an intrinsic mechanism to reduce variability of shifting segmentation patterns due to perturbations by maternal inputs, which is consistent with the increased variability of the posterior Hb boundary in *Kr* and *kni* double mutants (8). Together, these findings suggest that neither maternal factors nor the gap genes alone are sufficient for the reduction of the boundary variability; instead, a collective synergy of the entire segmentation gene network is needed. More interestingly, the observed dynamic adjustment mechanism suggests that this network integrates positional information from different maternal factors not by a direct molecular interaction at a particular time point of readout but via a dynamic interplay among the downstream components that occurs at a slightly later stage and also on a slower time scale.

According to a faithful, simple threshold-dependent readout (*SI Materials and Methods* and Fig. S1*A*), the concentration at a boundary position on altered Bcd dosage should be unchanged. However, we observe that the relative Bcd concentration at the location of the CF is higher than expected for increased Bcd dosage, and vice versa (Fig. 2C). Quantitatively, it follows a quasilinear relationship $\ln(C(x_{CF})/C^R(x_{CF})) = S_c * \ln D$ with a slope of $S_c = \sim 40\%$ instead of 0% as predicted by the simple threshold model. Sixty-three percent of this discrepancy can be attributed to the observed dynamical adjustment, as demonstrated by the adjusted relative Bcd concentration at the Hb boundary and at the position of Eve–Stripe-1 during n.c. 14 (Fig. 3*F*, *Inset*). Multiple scenarios are possible for the remaining 37%. The observed dynamics of the downstream genes are prone to begin earlier than at 10 min into n.c. 14, when we can measure them reliably (during n.c. 13, when boundaries are significantly shallower, we were unable to measure with sufficient accuracy and our data remain inconclusive), making them likely major contributors to the observed discrepancy. Nevertheless, we expect the total contribution of the dynamics to be less than ~80%. In the case of the maternal mutants, when no dynamic adjustments are observed, S_c is still ~9% (Fig. S6*C*), setting a bound on the impact of the dynamics. The remaining discrepancy could result from, for example, combining multiple inputs from a system of repressors for Bcd-regulating genes (5) or a pre–steady-state decoding of Bcd gradients (40). Both mechanisms could contribute to reduce the variability of the segmentation patterns on Bcd dosage perturbations before the dynamic adjustment mechanism is engaged. Future experiments will be needed to clarify if dynamic adjustments, the repressor system, and pre–steady-state decoding are indeed mechanistically unrelated or if they are, in fact, dependent on the combinatorial influence of the maternal products.

Even though our data indicate that the initial response to Bcd could be consistent to within less than 10% with an absolute concentration-dependent readout acting above a predefined threshold

(6), the subsequent dynamic adjustment of the boundary location suggests that the Bcd concentration at the final location is no longer relevant; it was the Bcd concentration at the earlier time point when it was first read out that most mattered. Its influence on the network becomes less important as the activity of the gap genes kicks in. This supports the view that maternal gradients provide the initial spatial cues to a network of cross-regulatory interactions between otherwise self-organized downstream genes (5, 18). In this context, the measured precision of the input gradients, such as Bcd (28), remains intriguing, given that the downstream network could, in principle, correct for potential fluctuations (8, 9), as shown by our study. We speculate that something about the concentration set point at the early Bcd readout must be a critical cue for the system and will require further investigation.

The perturbations that we are able to measure here point to a fundamental and unique understanding about the interpretation of TF concentrations. We are able to observe such subtle effects only because we are applying a physics approach based on highly precise measurements to biological specimens. For example, improvements in imaging were necessary to see nuclei containing Bcd-GFP all the way to the posterior end, leading to a dramatic reduction in systematic errors in low nuclear Bcd concentration measurements. Because of this reduction, we were able to show that gradient reproducibility is greatly increased in the posterior half of the embryo, a major prerequisite, together with identical length constants and reproducibility across different fly lines (Fig. S3), for our dosage measurements.

The series of fly lines that we have generated with both large and very small changes in absolute Bcd concentrations will prove to be a very useful tool not only to study the general properties of protein gradients but to investigate quantitatively the responses of the ensuing genetic network. Quantification of the responses to subtle input concentration perturbations can finally lead us to establish very "fine-grained" quantitative models operating at the biophysical "TF-DNA level" (41), surpassing the qualitative "coarse-grained" model from the traditional genetic mutation experiment that always has the potential to cause severe network changes. Our study has provided unique challenges for modeling attempts of the segmentation gene network that can faithfully reproduce gap gene dynamics in a WT setting (9). Our data reveal boundary shifts of the gap genes under altered Bcd input dosage conditions and a dynamic readjustment of the shifted boundaries toward their WT locations. Current models (7, 9, 30, 40) cannot reproduce these features, and a new generation of models is necessary to account for all available data.

Materials and Methods

Both Bcd-GFP gradients and CF positions were measured with live imaging using two-photon microscopy. The expression profiles of Bcd target genes were detected on immunostained embryos. More details are provided in *SI Materials and Methods*.

ACKNOWLEDGMENTS. We thank S. Small for fly lines $2II_A$ and $2II_B$; M. Biggin for antibodies; and W. Bialek, H. Garcia, S. Little, S. Di Talia, T. Schupbach, A. Sgro, and E. Wieschaus for comments on the manuscript. This work was supported by National Institutes of Health Grants P50 GM071508 and R01 GM097275 and by Searle Scholar Award 10-SSP-274 (to T.G.).

1. Levine M, Davidson EH (2005) Gene regulatory networks for development. *Proc Natl Acad Sci USA* 102(14):4936–4942.
2. Porcher A, Dostatni N (2010) The bicoid morphogen system. *Curr Biol* 20(5): R249–R254.
3. Rogers KW, Schier AF (2011) Morphogen gradients: From generation to interpretation. *Annu Rev Cell Dev Biol* 27(1):377–407.
4. Löhr U, Chung HR, Beller M, Jäckle H (2009) Antagonistic action of Bicoid and the repressor Capicua determines the spatial limits of Drosophila head gene expression domains. *Proc Natl Acad Sci USA* 106(51):21695–21700.
5. Chen H, Xu Z, Mei C, Yu D, Small S (2012) A system of repressor gradients spatially organizes the boundaries of Bicoid-dependent target genes. *Cell* 149(3):618–629.
6. Wolpert L (1969) Positional information and the spatial pattern of cellular differentiation. *J Theor Biol* 25(1):1–47.
7. Papatsenko D, Levine M (2011) The Drosophila gap gene network is composed of two parallel toggle switches. *PLoS ONE* 6(7):e21145.
8. Manu, et al. (2009) Canalization of gene expression in the Drosophila blastoderm by gap gene cross regulation. *PLoS Biol* 7(3):e1000049.
9. Manu, et al. (2009) Canalization of gene expression and domain shifts in the Drosophila blastoderm by dynamical attractors. *PLOS Comput Biol* 5(3):e1000303.
10. Lacalli TC, Harrison LG (1991) From gradients to segments: Models for pattern formation in early Drosophila embryogenesis. *Semin Dev Biol* 2:107–117.
11. Jaeger J, Sharp DH, Reinitz J (2007) Known maternal gradients are not sufficient for the establishment of gap domains in Drosophila melanogaster. *Mech Dev* 124(2): 108–128.
12. Kraut R, Levine M (1991) Spatial regulation of the gap gene giant during Drosophila development. *Development* 111(2):601–609.
13. Jaeger J, et al. (2004) Dynamic control of positional information in the early Drosophila embryo. *Nature* 430(6997):368–371.
14. Jaeger J, et al. (2004) Dynamical analysis of regulatory interactions in the gap gene system of Drosophila melanogaster. *Genetics* 167(4):1721–1737.
15. Edgar BA, Odell GM, Schubiger G (1989) A genetic switch, based on negative regulation, sharpens stripes in Drosophila embryos. *Dev Genet* 10(3):124–142.
16. Surkova S, et al. (2008) Characterization of the Drosophila segment determination morphome. *Dev Biol* 313(2):844–862.
17. Ochoa-Espinosa A, Yu D, Tsirigos A, Struffi P, Small S (2009) Anterior-posterior positional information in the absence of a strong Bicoid gradient. *Proc Natl Acad Sci USA* 106(10):3823–3828.
18. Driever W, Nüsslein-Volhard C (1988) The bicoid protein determines position in the Drosophila embryo in a concentration-dependent manner. *Cell* 54(1):95–104.
19. Driever W, Nüsslein-Volhard C (1988) A gradient of bicoid protein in Drosophila embryos. *Cell* 54(1):83–93.
20. St Johnston D, Driever W, Berleth T, Richstein S, Nüsslein-Volhard C (1989) Multiple steps in the localization of bicoid RNA to the anterior pole of the Drosophila oocyte. *Development* 107(Suppl):13–19.
21. Little SC, Tkačik G, Kneeland TB, Wieschaus EF, Gregor T (2011) The formation of the Bicoid morphogen gradient requires protein movement from anteriorly localized mRNA. *PLoS Biol* 9(3):e1000596.
22. Struhl G, Struhl K, Macdonald PM (1989) The gradient morphogen bicoid is a concentration-dependent transcriptional activator. *Cell* 57(7):1259–1273.
23. Driever W, Nüsslein-Volhard C (1989) The bicoid protein is a positive regulator of hunchback transcription in the early Drosophila embryo. *Nature* 337(6203):138–143.
24. Gergen JP, Coulter D, Wieschaus E (1986) Segmental pattern and blastoderm cell identities. *Gametogenesis and the Early Embryo*, ed Gall JG (Liss, New York), pp 195–220.
25. Houchmandzadeh B, Wieschaus E, Leibler S (2002) Establishment of developmental precision and proportions in the early Drosophila embryo. *Nature* 415(6873):798–802.
26. Crauk O, Dostatni N (2005) Bicoid determines sharp and precise target gene expression in the Drosophila embryo. *Curr Biol* 15(21):1888–1898.
27. Holloway DM, Harrison LG, Kosman D, Vanario-Alonso CE, Spirov AV (2006) Analysis of pattern precision shows that Drosophila segmentation develops substantial independence from gradients of maternal gene products. *Dev Dyn* 235(11):2949–2960.
28. Gregor T, Tank DW, Wieschaus EF, Bialek W (2007) Probing the limits to positional information. *Cell* 130(1):153–164.
29. Gao Q, Finkelstein R (1998) Targeting gene expression to the head: The Drosophila orthodenticle gene is a direct target of the Bicoid morphogen. *Development* 125(21): 4185–4193.
30. Reinitz J, Mjolsness E, Sharp DH (1995) Model for cooperative control of positional information in Drosophila by bicoid and maternal hunchback. *J Exp Zool* 271(1): 47–56.
31. Markstein M, Pitsouli C, Villalta C, Celniker SE, Perrimon N (2008) Exploiting position effects and the gypsy retrovirus insulator to engineer precisely expressed transgenes. *Nat Genet* 40(4):476–483.
32. Lutz R, Bujard H (1997) Independent and tight regulation of transcriptional units in Escherichia coli via the LacR/O, the TetR/O and AraC/I1-I2 regulatory elements. *Nucleic Acids Res* 25(6):1203–1210.
33. Namba R, Pazdera TM, Cerrone RL, Minden JS (1997) Drosophila embryonic pattern repair: How embryos respond to bicoid dosage alteration. *Development* 124(7): 1393–1403.
34. Vincent A, Blankenship JT, Wieschaus E (1997) Integration of the head and trunk segmentation systems controls cephalic furrow formation in Drosophila. *Development* 124(19):3747–3754.
35. Dubuis JO, Samanta R, Gregor T (2013) Accurate measurements of dynamics and reproducibility in small genetic networks. *Mol Syst Biol* 9:639.
36. Janody F, Sturny R, Catala F, Desplan C, Dostatni N (2000) Phosphorylation of bicoid on MAP-kinase sites: Contribution to its interaction with the torso pathway. *Development* 127(2):279–289.
37. Lander AD (2011) Pattern, growth, and control. *Cell* 144(6):955–969.
38. Grossniklaus U, Cadigan KM, Gehring WJ (1994) Three maternal coordinate systems cooperate in the patterning of the Drosophila head. *Development* 120(11):3155–3171.
39. Jaeger J (2011) The gap gene network. *Cell Mol Life Sci* 68(2):243–274.
40. Bergmann S, et al. (2007) Pre-steady-state decoding of the Bicoid morphogen gradient. *PLoS Biol* 5(2):e46.
41. Wilczynski B, Furlong EEM (2010) Challenges for modeling global gene regulatory networks during development: Insights from Drosophila. *Dev Biol* 340(2):161–169.

Supporting Information

Liu et al. 10.1073/pnas.1220912110

SI Materials and Methods

Fly Stocks and Genetics. Six fly lines expressing the gene *egfp-*(*bicoid*) *bcd* (1) were chosen as the founder lines for the generation of the Bcd-GFP fly line library (Table S1). Endogenous *bcd* in all founder lines was substituted by bcd^{E1} mutant, which acts as a null allele (2). Among the six founder fly lines, one fly line termed $2X_A$ with an X-chromosomal insertion of P[*egfp-bcd*] has been characterized in a previous study (1), and was chosen as our reference fly line. The other five fly lines were generated as follows: $2II_A$ and $2II_B$ were generated using P[*egfp-bcd*] in a ϕC31 RMCE integration vector (3) targeting the second chromosomal landing sites e38F1A and e43F9A, respectively; $2II_C$ was generated by standard P-element–mediated transgenesis of P[*egfp-bcd*] and also chromosome II; and $2III_A$ and $2III_B$ were generated by mobilization of the original X-chromosomal Bcd-GFP transgene in fly line $2X_A$ (1) on the third chromosome. The heterozygous fly lines with only a single copy of the *bcd* gene were generated by crossing females from the founder lines to males from fly line *yw;+;* bcd^{E1},p^p/*TM3*. The fly lines with multiple insertions of P[*egfp-bcd*] were generated by crossing the founder lines with multiply balanced fly lines, such as *egfp-bcd;Sp/CYO;Dr/TMS,sb*. Oregon-R WT was used as a control in the live imaging experiment to measure the background. Fly lines mutant for the maternal factors Torso-like (Tsl) or Nanos (Nos) were generated by crosses between the Bcd-GFP fly lines to BNT(*yw;+;* $bcd^{E1}nos^{BN}tsl^{-}$/*TMS,hs,sb*), BT (*yw;+;* $bcd^{E1}tsl^{-}$/*TMS,hs,sb*), and BN(*yw;+;* $bcd^{E1}nos^{BN}$/*TMS,hs,sb*) (4–6). Note that these fly lines were extremely difficult to generate and to maintain, especially in backgrounds of higher than endogenous Bcd dosage. Progeny of these crosses were heat-shocked (37 °C for 1 h) on day 5 after egg deposition and allowed to develop at 22 °C. The surviving homozygous females were collected and set up onto egg collection plates for imaging experiments of their embryos.

Live Imaging. Embryo preparation for live imaging was as reported earlier (7), except that the mounting orientation was changed to the dorsal side facing up, closest to the imaging objective of an upright microscope. To reduce orientation variation during the mounting process, 200-μm glass spacers were used to prevent mechanical stress when pushing the glass slide with glue on the embryos. Typically, the imaging for Bcd gradient measurement and cephalic furrow (CF) measurement was performed after 16 ± 2 min and 67 ± 2 min after entry into mitosis 13 (estimated by the disappearance of Bcd-GFP–filled nuclei), respectively. Live imaging was performed with a previously described custom-built, two-photon, point-scanning microscope (1), except that for fluorescence detection, a highly sensitive gallium-arsenide-phosphide (GaAsP) photomultiplier tube (module H10770PA-40 SEL; Hamamatsu) with dark counts smaller than 4,000 cps at 25 °C was used. The excitation wavelength was 970 nm, and average laser power at the specimen was 25 mW. Images were taken with a Zeiss 25× (N.A. = 0.8) oil/water-immersion objective. Microscope control routines (8) and all our image analysis routines were implemented using MATLAB software (MathWorks). For each embryo, three images [512 × 512 pixels, with 16 bits at 6.4 μs per pixel (4 ms per line)] were taken along the anterior-posterior (AP) axis (focused at the midcoronal plane) at magnified zoom (linear pixel dimension corresponds to 0.46 μm) and then stitched together in software; each image was an average of three sequentially acquired frames (Figs. 1*A* and 2*A*).

Identification of Nuclei in Live Images. The centroids of the nuclei were detected by searching for the peak intensity in a 7 × 7-pixel array around the center of the nuclear mask detected with a difference-of-Gaussian filter. The average nuclear fluorescence intensity was computed over a circular window of fixed size (diameter of 12 pixels). Embryos imaged at the midcoronal plane contained, on average, about 80 nuclei along each side, and roughly 60–70 of these nuclei could be detected automatically. The fluorescence background (green line in Fig. 1*B*) measured on WT embryos without Bcd-GFP expression is nearly zero and less than 20% of the nuclear Bcd-GFP fluorescence intensity at the posterior end. This low autofluorescence background is comparable to the dark counts in the image outside the embryo region.

Bcd-GFP Dosage Measurements. For each embryo, the nuclei detected from both sides were binned together with a bin size of 1% embryo length (EL) to obtain an average Bcd-GFP gradient along the AP axis for an individual embryo. To obtain the average Bcd-GFP gradient and its reproducibility for a given fly line, all nuclei detected in all embryos of the same fly line measured in a single imaging session were binned with a bin size of 1%EL, and the mean and SD for each bin were computed. Two types of dosage calculations were performed:

i) The relative dosage of individual embryos was computed by a linear fit to the scatter plot of the single embryo gradient vs. the average Bcd-GFP gradient of the reference fly line $2X_A$ measured in the same imaging session (Fig. 1*D*). To avoid fitting artifacts at the anterior and posterior poles, only data points within 10–80%EL were included in the fit.

ii) The average dosage of a fly line was computed by the linear fit to the scatter plot of the average Bcd-GFP gradient of that fly line vs. the average Bcd-GFP gradient of the reference fly line $2X_A$ measured in the same imaging session (Fig. 1 *E* and *F*).

For each dosage determination, measurements with at least 10 sample and 10 reference embryos were repeated over at least three independent imaging sessions. The mean value of the slopes was reported as the Bcd-GFP dosage of the sample fly line; its SD was determined by bootstrapping. The gradient intensity ratios of fly lines with different Bcd dosages remain constant over the time window from nuclear cycle (n.c.) 13 to late n.c. 14 (Fig. S3*C*); thus, relative Bcd dosages calculated with Bcd-GFP gradients measured 16 min after the start of n.c. 14 apply to the entire developmental process.

Error Propagation for Arithmetic Test. For the heterozygous fly lines derived from a founder fly line A with Bcd-GFP dosage $|A| \pm \delta|A|$ (where $\delta|A|$ is the measured SD), we computed the expected Bcd-GFP dosage and its SD as $|A|/2 \pm \delta|A|/2$. For a fly line generated by combining two different founder lines A and B with dosages $|A| \pm \delta|A|$ and $|B| \pm \delta|B|$, respectively, the expected Bcd-GFP dosage of the fly line $A + B$ is $|A+B| \pm \sqrt{(\delta|A|)^2 + (\delta|B|)^2}$, assuming the dosage measurements of the two founder lines are independent. The calculated expected Bcd-GFP dosages are shown as the horizontal error bars in Fig. 1*G*.

Live Imaging Measurement Noise of Bcd-GFP Concentrations. Gradient measurements are significantly improved over previous live imaging results (7) due to a substantial improvement of our imaging setup. This is demonstrated by the fact that we can detect nuclei containing Bcd-GFP all the way to the posterior end, which was not possible before, and by the fact that the embryo-to-embryo reproducibility in the anterior and posterior halves is at a

similar level. For inevitable residual experimental errors for Bcd dosage measurements, we identified six different sources of measurement noise:

i–iii) Imaging noise, nuclear identification noise, and focal plane adjustment noise as reported previously (7)

iv) Rotational asymmetry around the AP axis. Embryos are not rotationally symmetrical around the AP axis. To minimize the systematic error stemming from our inability to mount all embryos at the same azimuthal angle, we only selected embryos with near-perfect left-to-right symmetry that is given only in a dorsal view of the embryo, which was quantified by the intensity ratios between the left and right Bcd gradients. Only when this ratio was within 20% of unity did we retain the embryo for further analysis. The mean and SD of the ratios of the left and right gradients of the selected 968 embryos of reference fly line $2X_A$ are 0.94 ± 0.05.

v) Rotational asymmetry around the left-to-right axis. Because the embryos were mounted on their curved ventral side, there was significant variability due to the rotational angle around the left-to-right axis. Misorientation stemming from this artifact can be easily spotted by faint membrane segments in the anterior and posterior pole regions. We identified three classes of embryos based on the range of these faint membrane segments: low (<1%EL), medium (<3%EL), and high (>3%EL). We only selected embryos that were devoid of such faint segments (low class), and we estimated the upper bound of the systematic measurement error due to this rotational angle to be of the order of 5% (i.e., the average deviation from unity of the relative dosage of individual embryos in the medium class).

vi) Sample size. Dosage measurements are typically made with sample sizes of at least 10 embryos per fly line per imaging session. For that case, the dosage measurement error is ~6% [using error propagation on the ratio of two fly lines with a SEM of 4% (as discussed in the main text) and assuming the measurement errors of the reference and sample fly line are independent].

Live Imaging Measurement Noise of CF Positions. For CF measurements (Fig. 2 *A* and *B*), we identified five different sources of measurement noise:

i) Measurement time uncertainty. The measured CF position shifts as development progresses are shown in Fig. S5*A*, and the estimated measurement error contributed from this source is ~0.35%.

ii) Focal plane adjustment noise. Measurements of CF positions in the z-stacks around the midcoronal plane (Fig. S5*B*) allowed us to estimate the measurement error from this source to be ~0.35%.

iii) Rotational around left-to-right axis. CF positions are independent of the rotational angle around the AP axis but depend on the rotation around the left-to-right axis. We classified embryos into three groups as described in the previous section. The upper bound for our CF measurement error from this source is 0.5%EL (the average deviation of the CF position of the medium class from the mean CF position of the low class).

iv) Nuclear shift. The nuclei shift posteriorly in the anterior region at the onset of CF formation. We estimated the measurement error from this source to be ~0.6%EL by quantifying the variance of the distance between the anterior tip of the embryo membrane and the anterior-most nuclei (Fig. S5*C*).

v) Image processing. CF locations were identified by manually clicking the center of the furrow gap (red dots in Fig. 2*A*). The resulting measurement error from this image processing step is ~0.23%EL (Fig. S5*D*).

Antibody Staining and Confocal Microscopy. All embryos were collected at 25 °C, heat-fixed, and labeled with fluorescent probes. Primary antibodies used were rat anti-Hunchback (Hb), guinea pig anti-Giant (Gt), rabbit anti-Krüppel (Kr), rabbit anti–Even-Skipped (Eve), and rabbit anti-Bcd (provided by Mark Biggins, Lawrence Berkeley National Laboratory, Berkeley, CA). Secondary antibodies used were Alexa Fluor 647 goat anti-rabbit IgG, Alexa Fluor 594 goat anti-guinea pig IgG, and Alexa Fluor 488 goat anti-rat IgG (AlexaFluor). For nuclear identification, all embryos were also stained with DAPI. Embryos were mounted in AquaPolymount (Polysciences, Inc.) with spacers between the slide and coverslip to minimize flattening. High-resolution digital images (1,024 × 1,024, 12 bits per pixel) of fixed eggs were obtained on a Leica SP-5 confocal microscope with a 20×/0.7-N.A./glycerol objective. The image focal plane was chosen at the midsagittal plane for protein profile extraction (Fig. S7*A*).

Correction for EGFP Maturation in Live Bcd-GFP Measurements. Because it takes tens of minutes for EGFP to mature, only a fraction of Bcd-GFP is visible in living embryos (9, 10). To obtain the actual Bcd-GFP concentration from the live Bcd-GFP measurement, we determined a maturation correction factor by fitting calculated Bcd-GFP gradients to measured Bcd-GFP gradients in both living and fixed embryos (Fig. S4 *A* and *B*). According to the synthesis-diffusion-degradation (SDD) model (1, 7, 11), the dynamics of the Bcd-GFP gradient can be described by $\frac{\partial C_{tot}(x,t)}{\partial t} = D * \nabla^2 C_{tot}(x,t) - 1/\tau_d * C_{tot}(x,t) + j_0\delta(x)$, where $C_{tot}(x,t)$ represents the total Bcd-GFP concentration, namely, the sum of the mature, visible Bcd-GFP ($C_m(x,t)$) and immature, dark Bcd-GFP ($C_{im}(x,t)$) in live Bcd-GFP measurements. D is the diffusion constant, τ_d is the degradation time, and j_0 is the Bcd-GFP synthesis rate. The steady-state solution of this equation is given by $C_{tot}(x) = C_0 e^{-x/\lambda}$ with $C_0 = j_0/\sqrt{D/\tau_d}$ and $\lambda = \sqrt{D*\tau_d}$. $C_{tot}(x)$ can be measured in fixed embryos, either directly with EGFP fluorescence (10) or after immunostaining for EGFP or Bcd (the latter is used in this work). For the immature Bcd-GFP contribution alone, the gradient dynamics also follow the SDD model except that $1/\tau_d$ has to be replaced by $1/\tau_d + 1/\tau_m$, where τ_m is the maturation time of EGFP. Thus, the steady-state gradient of immature Bcd-GFP is given by $C_{im}(x) = C_0 * k * e^{-x/(k*\lambda)}$, where $k = \sqrt{\tau_m/(\tau_d+\tau_m)}$. The Bcd-GFP contribution with mature EGFP follows from the difference $C_m(x) = C_{tot}(x) - C_{im}(x)$, and is the actual magnitude that is measured in living embryos. To determine the parameter k, we fit $C_{tot}(x)$ and $C_{im}(x)$ to the measured average Bcd-GFP gradients in fixed and living embryos from the reference fly line $2X_A$, respectively. The average Bcd-GFP gradients were calculated by selecting fixed embryos with the same orientation (dorsal view) and similar embryo age as the measured living embryos [16 ± 5 min into n.c. 14, determined by the invagination depth of the membrane furrow canals (12)]. At the chosen embryo age, Bcd-GFP gradients reach their steady state (1, 10). To reduce the number of fitting parameters, the background and amplitude of the raw intensity were corrected. The measured fluorescence intensity of Bcd-GFP can be described by $I(x) = G * C(x) + B$, where $C(x)$ is the measured Bcd-GFP concentration, G is the imaging gain factor, and B is the imaging background. B was estimated for living embryos by measuring WT embryos under the same imaging conditions. For fixed embryos, we fitted the raw intensity profile of the gradient with the formula $Ae^{-x/\lambda} + B$. After background subtraction, the amplitudes of the gradients were adjusted by multiplying with a factor to match the gradient intensity in the posterior region ($x/L = 0.8$–0.9), assuming that all Bcd-GFP molecules in that region have mature EGFP (Fig. S4*A*). We found that $k = 0.7$ yields the best fit of the calculated gradients to their corresponding measured gradients: $C_{tot}(x)$ vs. Bcd-GFP fixed and $C_{im}(x)$ vs. Bcd-GFP live (Fig. S4*C*). The resulting τ_d/τ_m ratio is ~1, indicating

that the lifetime of Bcd-GFP is of the same order as the maturation time of EGFP in the embryo. Given the measured lifetime of Bcd-Dronpa [i.e., $\tau_d \cong 50$min (9)], the above ratio implies that the maturation time of EGFP is ~50 min, which is consistent within the range of currently estimated values in fly embryos (9, 13). Finally, the maturation correction factor for live Bcd-GFP measurement is given by $R_M(x) = C_{tot}(x)/C_m(x)$, using $k = 0.7$ (Fig. S4*D*). It is an AP position-dependent factor with a maximum value of about 3 at the anterior pole and a minimum value of nearly 1 at the posterior pole.

Determination of the Bcd-GFP Concentration at the CF Position. The concentration at the location of the CF [$C(x_{CF})$] can be expressed as $C(x_{CF}) = C_D e^{-x_{CF}/\lambda}$,where C_D and λ are the amplitude and length constants of the Bcd-GFP gradient, respectively. To calculate $C(x_{CF})$, several steps are necessary to convert the raw intensity of the Bcd-GFP gradient, $I(x)$, from live imaging to Bcd-GFP concentration $C_{tot}(x)$. First, the background B is subtracted from $I(x)$ (see the section above). Then, the intensity is converted to Bcd-GFP concentration using the measured imaging gain factor G. Based on in situ Bcd-GFP concentration calibration (7), $G = I^R_{ave}/8$nM, where I^R_{ave} is the intensity of the average Bcd-GFP gradient of the reference fly line $2X_A$ at location $x/L = 0.48$. The mature contribution (C_m) of Bcd-GFP as measured with live imaging can be calculated as $C_m(x) = (I(x) - B)/G$. Finally, we used the maturation correction factor to calculate the total Bcd-GFP concentration $C_{tot}(x) = C_m(x) * R_M$ (see the section above). We extracted C_D and λ from linear fits of $ln(C_{tot}(x))$ vs. x. Given the slope m and the intercept y_0, $\lambda = 1/m$ and $C_D = exp(y_0)$. To avoid fitting artifacts at the anterior and posterior poles, only data points within the 20–80%EL range were included in the fits. The $C(x_{CF})$ of all embryos of the sample fly line was normalized by $C^R(x_{CF})$, the mean value of $C(x_{CF})$ of the reference fly line $2X_A$, measured in the same imaging session. Fig. 2*C* shows the relative $C(x_{CF})$ vs. Bcd dosage D. As a control, we also extracted the concentration of nuclear Bcd-GFP $C(x_{CF})$ at the location of the CF, x_{CF} from the corresponding Bcd-GFP concentration gradient by choosing the location of a measured nucleus closest to x_{CF} measured in the same embryo (Fig. S6*A*). Due to the measurement noise in both the determination of x_{CF} and the nuclear Bcd-GFP concentrations, the resulting SD on relative $C(x_{CF})$ is 16 ± 5% for the 19 sample fly lines, which is slightly higher than the 14 ± 4% that we computed using C_D and λ from the fits. Nevertheless, we observe the same quasilinear relationship between the relative $C(x_{CF})$ and Bcd dosage D on a log-log scale with both methods, with a slope S_c of 44 ± 2% (Fig. 2*C*) and 42 ± 2% (Fig. S6*A*), respectively.

Connection Between CF Position, Bcd Concentration, and Bcd Dosage. How the CF position responds to the imposed Bcd dosage perturbations can be described either by a concentration representation [i.e., $C(x_{CF})$ vs. D (Fig. 2*C* and Fig. S6*A*)] or by a position representation [i.e., x_{CF} vs. D (Fig. S6*B*)]. We can establish a mathematical connection between the two representations to show that the observed quasilinear relationship between $\ln(C(x_{CF})/C^R(x_{CF}))$ and $\ln(D)$ (see the section above) can be predicted from the quasilinear relationship $x_{CF} = S_x\ ln(D) + x^R_{CF}$, as observed in Fig. S6*B*, where S_x is the slope of the linear fit. Combining this formula for $x_{CF}(D)$ with $C(x_{CF}) = C_D e^{-x_{CF}/\lambda}$, and $D = \frac{C_D}{C^R_D}$, where C^R_D is the amplitude of the Bcd-GFP gradient of the reference fly line, we obtain $C(x_{CF})/C^R(x_{CF}) = D^{S_c}$, with $S_c = 1 - \frac{S_x}{\lambda}$. From our data, we infer that $\lambda = 16.5$ ± 0.7%EL and $S_x = 10.5$ ± 0.2%EL (dark solid line in Fig. S6*B*); thus, we predict that $S_c = 36 \pm 2\%$, which is very close to the measured value of the slope $S_c = 44 \pm 2\%$ in Fig. 2*C* (dotted line). Most of the discrepancy between the two values comes from an ~10% increase of λ as Bcd dosage D increases from 0.44 to 2.4 (Fig. S3*A*). Thus, the measured dependence between $C(x_{CF})$ and Bcd dosage D is quantitatively consistent with the measured dependence between x_{CF} and Bcd dosage D. This consistency also validates our calculation of $C(x_{CF})$, because we can derive its dependence on D directly from the raw data given by x_{CF} vs. D in Fig. S6*B*. With these two different representations, we demonstrate that the observed response of the CF position to Bcd dosage perturbations is quantitatively different from the two scenarios illustrated in Fig. S1. In the scenario following the traditional threshold-dependent readout model with $S_c = 0$ in Fig. S1*A*, we have $C(x_{CF}) = C^R(x_{CF})$, and the Bcd concentration at x_{CF} is a constant (dashed line in Fig. 2*C*), corresponding to the linear relationship $x_{CF} = \lambda lnD + x^R_{CF}$ (dashed line in Fig. S6*B*). In the alternative scenario with $S_c = 1$ (Fig. S1*B*), we have $\frac{C(x_{CF})}{C^R(x_{CF})} = D$, and the Bcd concentration at the CF location is proportional to the overall Bcd dosage (dashed-dotted line in Fig. 2*C*), corresponding to the constant function $x_{CF} = x^R_{CF}$ (dashed-dotted line in Fig. S6*B*). Hence, S_c can be used as an indicator to quantify how much the Bcd concentration readout at a patterning marker's position deviates from the prediction of the threshold-dependent readout model. As for the CF, we can show that S_c, in fact, measures the percent reduction of the spatial CF shift with respect to the amount predicted by the threshold-dependent model. The actual shift of the CF is given by $\Delta x_{CF} = x_{CF} - x^R_{CF} = S_x lnD = \lambda(1 - S_c) lnD$ (instead of $\Delta x_{CF} = \lambda lnD$, as predicted by the threshold-dependent model). Thus, the observed shift is reduced by $\lambda S_c lnD$, and the percentage of this reduction with respect to the predicted amount λlnD is S_c.

Quantification of Bcd-GFP Concentrations at Gene Expression Boundaries. The Hb, Gt, Kr, and Eve protein profiles were extracted from confocal images of immunostained embryos using MATLAB software routines that allowed a rectangle window of the size of a nucleus to be systematically moved along the band of nuclei within the embryo as described previously (12). At each position, the average pixel intensity within the window was plotted vs. the projection of the window center along the AP axis of the embryo. The AP axis was defined as the major axis of the embryo mask. Protein profile measurements were made separately along the dorsal and ventral sides of the embryo (Fig. S7*B*). The boundaries of the Hb, Gt, and Kr anterior expression domains were detected at their location of half-maximal intensity with an estimated measurement error of ~0.6% EL (Fig. S8*A*). Identification of seven local profile expression maxima determined the peak positions of Eve stripes. All automatically detected marker positions were manually verified (Fig. S8*C*). To minimize the measurement error from embryo orientation, marker positions were calculated as the average values of the positions from the dorsal and ventral sides for individual embryos (Fig. S8*B*) and only embryos imaged from a lateral view were chosen for data analysis. Embryo age was measured using the invagination depth of the membrane furrow canals during n.c. 14 (12). Under these stringent controls on embryo age and orientation, the SD of the Hb boundary and Eve peaks is less than 1%EL (Fig. S8), approaching the biological noise limit (12). Bcd-GFP concentrations at the detected marker positions were calculated with the same method as described above for $C(x_{CF})$ except that we used the average Bcd-GFP gradient of the respective fly line [instead of the Bcd-GFP gradient of the corresponding single embryo as was the case for our $C(x_{CF})$ calculations]. Given the high reproducibility of the Bcd-GFP gradients, the error in the thus calculated Bcd-GFP concentrations at these marker positions is less than 15%, which is well below the observed dynamic concentration changes between early and late time points in n.c. 14. Note that the changes of Bcd concentrations at the marker positions of these expression patterns are even smaller than in the case of the CF, and they evolve over time. Such small effects can only be revealed by a measurement protocol that is precise and accurate (i.e., where we understand the various sources of measurement noise) (12).

1. Gregor T, Wieschaus EF, McGregor AP, Bialek W, Tank DW (2007) Stability and nuclear dynamics of the bicoid morphogen gradient. *Cell* 130(1):141–152.
2. Frohnhöfer HG, Nüsslein-Volhard C (1986) Organization of anterior pattern in the Drosophila embryo by the maternal gene bicoid. *Nature* 324:120–125.
3. Bateman J, Lee A, Wu C (2006) Site-specific transformation of Drosophila via PhiC31 integrase-mediated cassette exchange. *Genetics* 173:769–777.
4. Wang C, Dickinson LK, Lehmann R (1994) Genetics of nanos localization in Drosophila. *Dev Dyn* 199(2):103–115.
5. Savant-Bhonsale S, Montell DJ (1993) torso-like encodes the localized determinant of Drosophila terminal pattern formation. *Genes Dev* 7(12B):2548–2555.
6. Tearle RG, Nusslein-Volhard C (1987) Tubingen mutants and stock list. *Drosophila Information Server* 66:209–269
7. Gregor T, Tank DW, Wieschaus EF, Bialek W (2007) Probing the limits to positional information. *Cell* 130(1):153–164.
8. Pologruto TA, Sabatini BL, Svoboda K (2003) ScanImage: Flexible software for operating laser scanning microscopes. *Biomed Eng Online* 2:13.
9. Drocco JA, Grimm O, Tank DW, Wieschaus E (2011) Measurement and perturbation of morphogen lifetime: Effects on gradient shape. *Biophys J* 101(8): 1807–1815.
10. Little SC, Tkačik G, Kneeland TB, Wieschaus EF, Gregor T (2011) The formation of the Bicoid morphogen gradient requires protein movement from anteriorly localized mRNA. *PLoS Biol* 9(3):e1000596.
11. Grimm O, Coppey M, Wieschaus E (2010) Modelling the Bicoid gradient. *Development* 137(14):2253–2264.
12. Dubuis JO, Samanta R, Gregor T (2013) Accurate measurements of dynamics and reproducibility in small genetic networks. *Mol Syst Biol* 9:639.
13. Di Talia S, Wieschaus EF (2012) Short-term integration of Cdc25 dynamics controls mitotic entry during Drosophila gastrulation. *Dev Cell* 22(4):763–774.

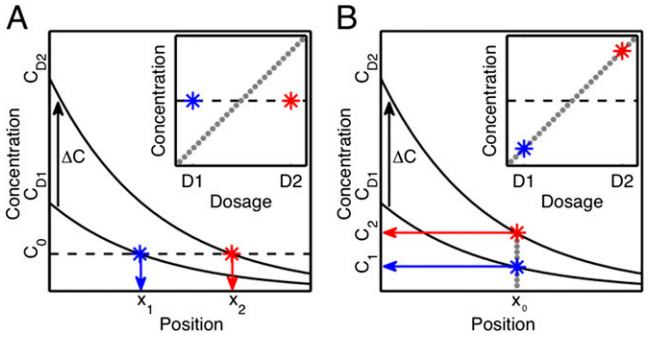

Fig. S1. Are concentration changes equivalent to changes in position? For two fly lines 1 and 2 with Bcd dosages *D1* and *D2*, the Bcd concentration profile can be described at steady state by a 1D decaying exponential $C(x) = C_D e^{-x/\lambda}$, where x represents the position from the anterior pole, C_D is the gradient amplitude, and λ is the gradient's shape-determining length constant. In fly line 1, the position x_1 of a specific marker (e.g., the CF) is determined at an effective Bcd concentration C_0 (effective because the readout may not be direct). (*A*) If changing concentration and changing position are indeed equivalent, we should then see in fly line 2, whose overall concentration is increased by ΔC, a new location x_2 for the same marker, also determined at C_0, as illustrated. (*B*) Opposite scenario is depicted, where the marker location x_0 is independent of overall concentration changes; hence, the effective readout concentration changes from C_1 to C_2 in the two fly lines. (*A* and *B*, *Insets*) Bcd concentration at the marker positions for fly lines 1 and 2 (blue and red, respectively) as a function of Bcd dosage *D*. Lines represent identical scenarios as in the main figure: The black dashed line corresponds to a scenario where the readout concentration does not change in the different dosage backgrounds, and the gray dotted line corresponds to a scenario where the marker position is independent of overall concentration changes (concentration is linearly proportional to dosage) (*SI Materials and Methods, Connection Between CF Position, Bcd Concentration and Bcd Dosage*).

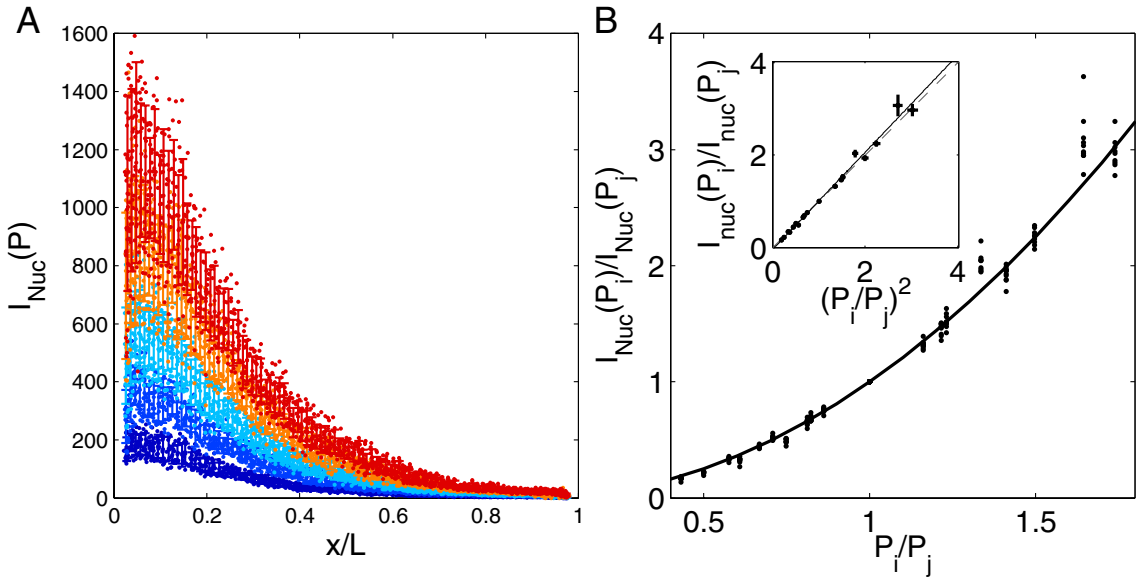

Fig. S2. Bcd dosage measurement control at different excitation powers. (*A*) Nuclear Bcd-GFP intensity, $I_{Nuc}(P)$, of 10 embryos of the reference fly line $2X_A$ taken at five different excitation powers (P_i = {15, 20, 25, 30, 35} mW at the specimen). Each color represents a different power. Error bars are the means and SDs of pooled nuclei in 100 equidistant bins. (*B*) Scatter plot of the nuclear Bcd-GFP fluorescence intensity ratio, $I_{Nuc}(P_i)/I_{Nuc}(P_j)$ shown in *A* vs. the excitation power ratio P_i/P_j. All data points (black dots) fall on the expected parabola (black line; the fluorescence intensity is proportional to the square of the excitation power for two-photon microscopy). (*B*, *Inset*) Scatter plot of the measured I_{Nuc} ratio vs. the expected ratio (i.e., the square of the power ratio). Error bars are SDs. The slope of the linear fit (black line) is 1.05 ± 0.06. The gray dashed line shows the expected line with slope 1. This result indicates that our Bcd dosage measurements have a nearly perfect linearity in the dosage range of 0.4–3.0.

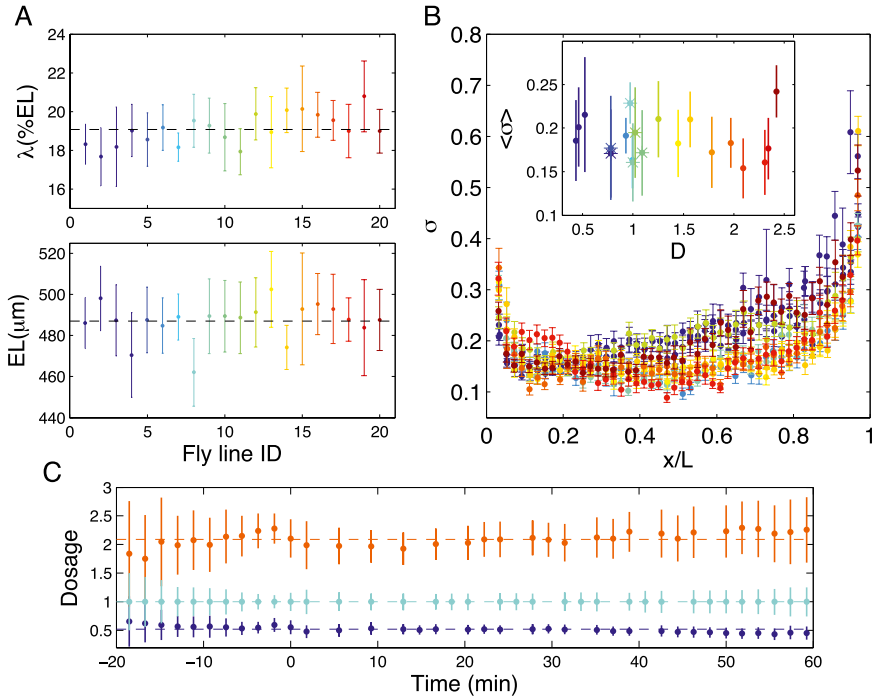

Fig. S3. Bcd-GFP gradient properties of 20 Bcd-GFP fly lines. (*A*) Means and SDs of the length constants λ (*Upper*) and embryo lengths (EL; *Lower*) of the sets of Bcd-GFP gradients of 20 Bcd-GFP fly lines listed in Table S1. The gradient length constants of the different lines are almost identical to the reference fly line with a mean and SD across the 20 fly lines of 19.1 ± 0.8%EL. Note that in our live Bcd-GFP measurements, delayed EGFP maturation alters the shape of the Bcd gradient slightly. The mean length constant was reduced to 16.5 ± 0.7%EL after corrections for EGFP maturation (*SI Materials and Methods*). (*B*) Relative variability of Bcd levels across embryos as a function of fractional embryo length for the 11 representative fly lines shown in Fig. 1*F*. The nuclei from 15 to 21 embryos per fly line were binned in 50 equidistant bins. The value of σ was calculated by dividing the SD of the nuclear intensity by the mean of each bin ($\sigma = \delta[Bcd]/[Bcd]$). Error bars were computed by bootstrapping. Colors correspond to fly line identification (ID) nos. in *A*. (*B*, *Inset*) Reproducibility of σ averaged over a spatial region $x/L = 0.2$–0.8 as a function of Bcd dosage D for 20 fly lines (ID nos. 1–20 in Table S1; founder lines are marked by stars). Error bars are SDs over that same region. Note the comparable levels of reproducibility across fly lines, guaranteeing the same measurement reliability for all dosages. (*C*) Time invariance of Bcd dosage measurements. Bcd dosages of fly line $1X_A$ (blue; ID = 3) and fly line $2X_A2III_A$ (orange; ID = 16) are shown as a function of time; reference fly line $2X_A$ (cyan; ID = 9) is measured concurrently for normalization. A time of 0 min is set at the onset of the 13th mitosis (evaluated by the disappearance of nuclear Bcd-GFP fluorescence). Error bars are SDs as described above. Dashed lines show the values of the expected dosage from measurement at 16 min.

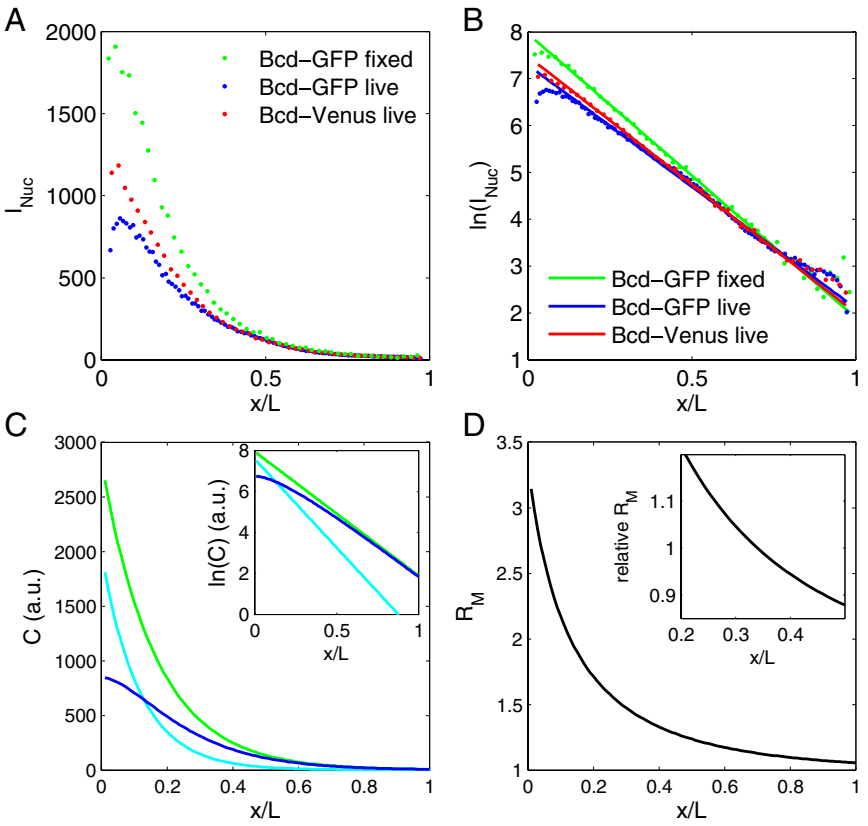

Fig. S4. EGFP maturation affects Bcd-GFP gradient measurements. (*A*) Comparison of I_{Nuc}, the binned nuclear fluorescence gradients averaged over 21 live $2X_A$ embryos expressing Bcd-GFP (blue dots, from Fig. 1*C*), 27 live embryos expressing Bcd-Venus (red dots), and 12 fixed $2X_A$ embryos immunostained for Bcd (green dots). (*B*) Log-linear (ln) plot of I_{Nuc} (fluorescence intensity of the Bcd gradients) vs. *x*/*L*. Colors for individual gradients are as in *A*. The length constants of the gradients obtained from linear fits to the data in the region *x*/*L* = 0.2–0.8 are 19.3%EL (blue), 18.2%EL (red), and 16.4%EL (green), respectively. (*C*) Steady-state Bcd-GFP concentration *C* vs. *x*/*L*. The total concentration C_{tot} (green line) is composed of the C_m (blue line, contributed by Bcd-GFP molecules with matured EGFP, which are visible with live imaging) and the immature contribution C_{im} (cyan line, contributed by Bcd-GFP molecules with immature EGFP, which are invisible for live imaging), assuming the degradation time of Bcd-EGFP is the same as the maturation time of EGFP (*SI Materials and Methods*). (*C*, *Inset*) Log-linear plot of these gradients. a.u., arbitrary units. (*D*) Relative maturation correction factor R_M calculated as the ratio of the gradient of total Bcd-GFP (green line in *C*) to matured Bcd-GFP (blue line in *C*) (*SI Materials and Methods*). (*D*, *Inset*) Relative maturation correction factor in the region *x*/*L* = 0.2–0.5 normalized by the maturation factor at the CF position of the reference fly line $2X_A$.

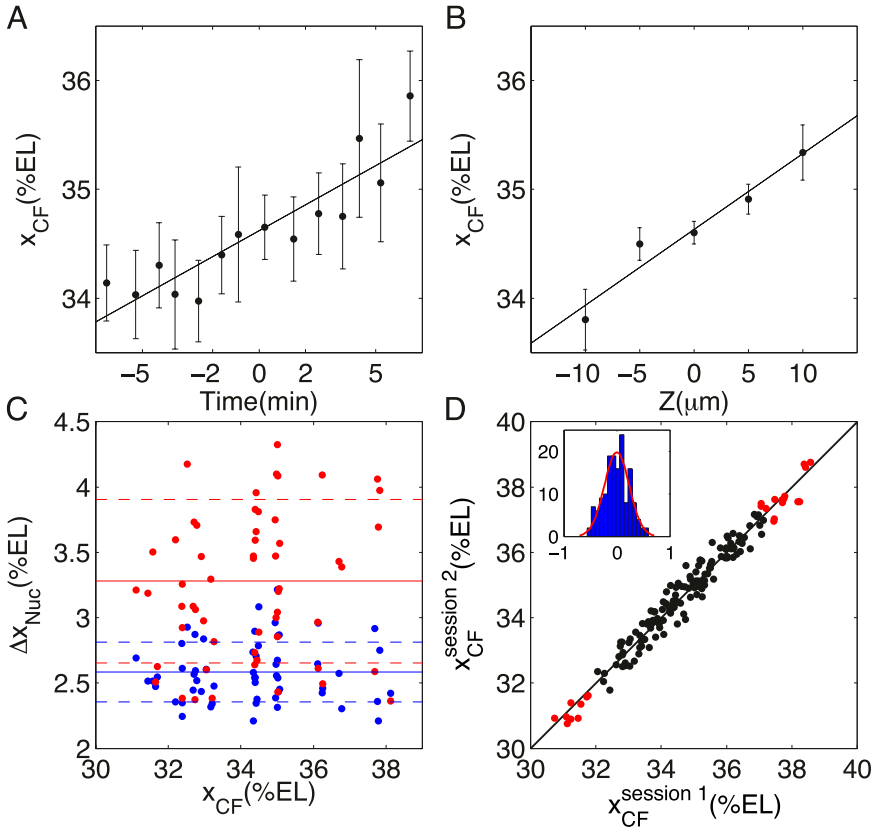

Fig. S5. CF measurement error analysis. (*A*) CF position shifts posteriorly as development progresses. Data points represent the mean and SE of x_{CF} [the CF positions of 12 $2X_A$ living embryos measured around the time point $t = 0$, at which time we typically record the CF position in our measurements (i.e., 67 ± 2 min after entry into mitosis 13, when, on average, 5 ± 1 nuclei had migrated into the interior of the embryo on both sides)]. The solid line shows a linear fit to these data, with a slope of 0.1%EL/min. We estimate the time window at which we typically record CF positions to be about ±2 min; thus, the measurement error resulting from our measurement time uncertainty is ∼0.35%EL. (*B*) CF position shifts posteriorly as the imaging plane moves from −10 μm below to 10 μm above the midcoronal plane ($Z = 0$ μm). Data points represent the mean and SE of x_{CF}, CF positions of 8 $2X_A$ embryos measured at $Z = \{-10, -5, 0, 5, 10\}$ μm. The solid line is a linear fit to the data, and its slope is 0.07% EL/μm. We estimate the inaccuracy for our midcoronal plane identification to be ∼5 μm; thus, the measurement error resulting from the focal plane adjustment uncertainty is ∼0.35%EL. (*C*) Collective nuclear shifts along the AP axis during gastrulation contribute to the CF measurement error. Data points are the distance between the anterior tip of the embryo membrane and the anterior-most nuclei (Δx_{Nuc}) of 56 $2X_A$ embryos as a function of CF position. Three subsets of the CF distribution in Fig. 2*B* were selected: 22 embryos from the small tail, 11 embryos from the large tail, and 23 embryos from the center of the distribution. Blue data points correspond to a time when the Bcd gradient was measured; red data points correspond to a time when the CF was measured. The mean of Δx_{Nuc} increases from 2.6%EL (blue solid line) to 3.3%EL (red solid line) between the two time points. The SD of Δx_{Nuc} increases from 0.2%EL to 0.6%EL (dashed lines represent mean ± SD). If the nuclei at the CF position have the same shift variance as the anterior-most nuclei, the CF position measurement error resulting from the nuclear shift is ∼0.6%EL. (*D*) Scatter plot of CF positions of 152 $2X_A$ embryos measured in two different sessions ($x_{CF}^{session2}$ vs. $x_{CF}^{session1}$) by manual identification of CF positions (outliers omitted in subsequent data analysis are shown in red). (*D*, *Inset*) Histogram of the CF position difference of the two measurements (least-square distance of data points from diagonal in the main panel). The red curve shows a Gaussian fit with an SD of 0.23%EL [i.e., our estimated measurement error from manually identifying the CF position (corresponding to ∼2.5 pixels in the raw images)].

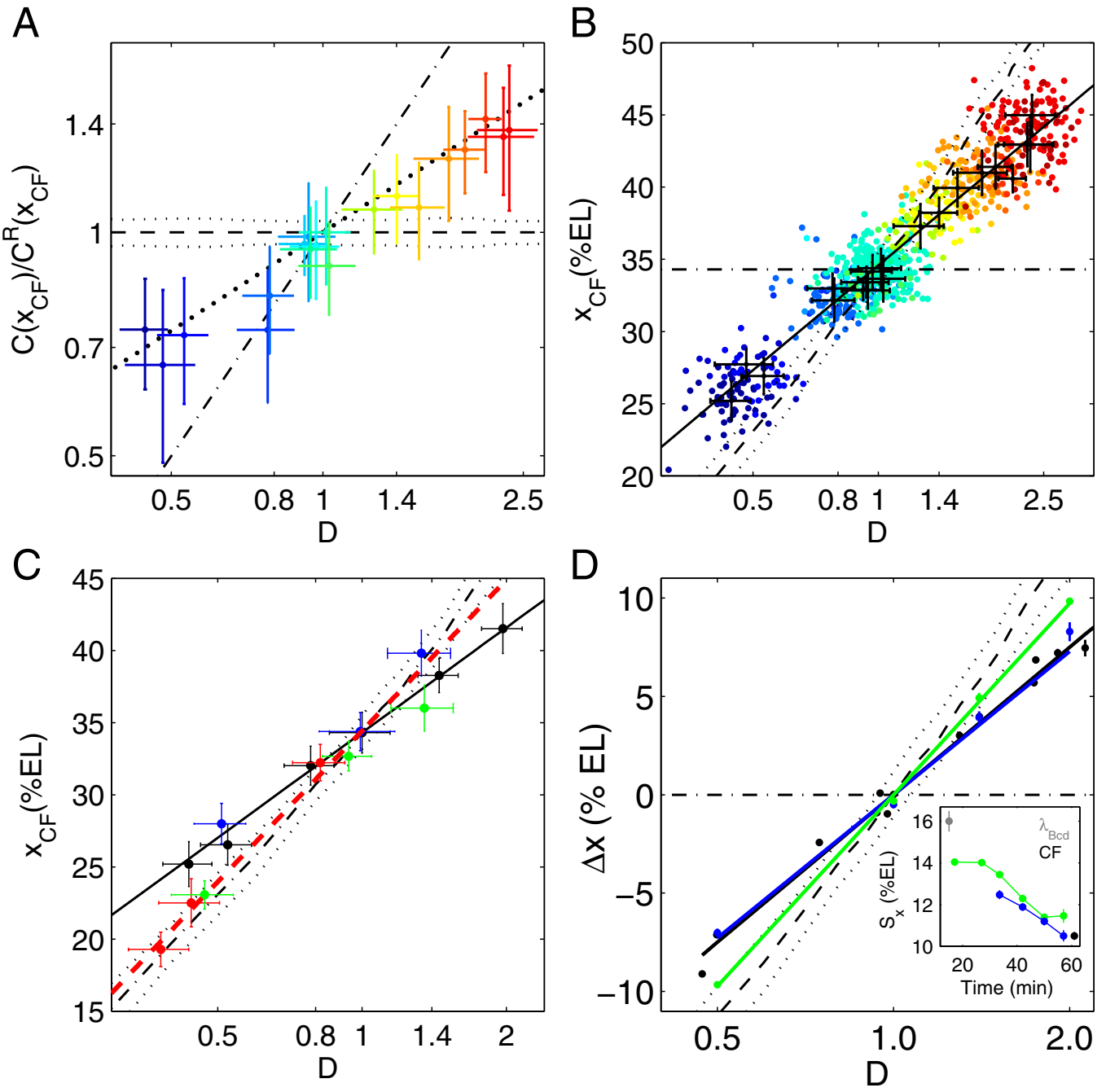

Fig. S6. CF position response to Bcd dosage perturbations. (*A*) Log-log plot of the Bcd-GFP concentration at the CF position, $C(x_{CF})$, normalized by $C^R(x_{CF})$ of the reference fly line $2X_A$ as a function of Bcd-GFP dosage *D* for 20 fly lines. This plot is equivalent to Fig. 2*C* except that each $C(x_{CF})$ is reported as the local reading of the measured Bcd-GFP concentration, as opposed to the concentration reading of the fitted gradients as in Fig. 2*C* (*SI Materials and Methods*). Hence, the SDs of the relative $C(x_{CF})$ are higher, largely due to measurement noise. We observed the same fold change as in Fig. 2*C*. (*B*) Linear-log plot of x_{CF} vs. Bcd-GFP dosage *D* for 20 fly lines. The complete dataset is shown; different colors represent different dosages, and each dot represents a measurement in a single embryo. Black crosses are the averages and SDs within a given fly line. The linear fit (dark solid line) to a total of 1,187 single embryo data points yields a slope of $S_x = 10.5 \pm 0.2\%$EL and an intercept at a WT dosage ($D = 1$) of $34.5 \pm 0.9\%$EL ($R^2 = 0.89$). The dashed-dotted line for reference is at WT CF location $x^R_{CF} = 34.3\%$EL. The dashed and dotted lines are the means and SDs of the predicted CF positions, respectively. The prediction is based on the maturation- and background-corrected Bcd-GFP gradients of 21 $2X_A$ embryos from live imaging (Fig. 1*C*) with the assumption that the Bcd concentration at x_{CF} is unchanged for fly lines with different Bcd dosages. Hence, for a sample fly line with Bcd dosage *D*, its CF position is predicted to be x^S_{CF}, where the Bcd-GFP intensity at x^S_{CF} should be equal to $I^R(x^R_{CF})$, the Bcd-GFP intensity of the reference fly line at x^R_{CF}. Because the sample fly line has almost the same length constant as the reference fly line $2X_A$ (Fig. S3*A*), its intensity can be approximated as $D * I^R(x)$. Thus, the predicted x^S_{CF} as a function of D can be calculated with the formula $D * I^R(x^S_{CF}) = I^R(x^R_{CF})$. The SD is calculated by bootstrapping. (*C*) Linear-log plot of x_{CF} vs. Bcd dosage *D* for fly lines carrying various copies of the Bcd-GFP transgene in maternal mutant backgrounds. Red, green, and blue symbols represent the means and SDs of the CF position and Bcd dosage of fly lines with maternal mutations $bcd^{E1}nos^{BN}tsl^{-}$, $bcd^{E1}tsl^{-}$ and $bcd^{E1}nos^{BN}$, respectively. The red dashed line is a linear fit to the red and green data points, and its slope is $S_x = 15.1 \pm 3.1\%$EL ($R^2 = 0.99$). This slope can be converted to $S_c = 9\%$ using the conversion $S_c = 1 - \frac{S_x}{\lambda}$, where $\lambda = 16.5\%$EL, the length constant of the Bcd gradient of the reference fly line $2X_A$. The black data (points, solid line, dashed line, and dotted line) are identical to those in *B*. (*D*) Representation of the dynamics of the

Legend continued on following page

marker position shifts Δx on Bcd dosage D perturbations. Each data point is the mean relative position normalized to the WT location of the three considered markers (Hb boundary, Eve–Stripe-1, and CF) as a function of Bcd dosage: Hb boundary at 10–24 min (green), Eve–Stripe-1 at 53–62 min (blue), and CF at 67 min (black). (Hb and Eve data are shown in Fig. S7 *C* and *G*.) They denote the beginning and the end of the observed dynamic boundary adjustment. Error bars represent SEMs. For each marker, the value of the fit at $D = 1.0$ is subtracted such that the different markers can all be compared in the same plot. The slopes of the linear fits to the data points of Hb, Eve1, and CF are $S_x = 14\%$, 10.5%, and 10.5%, respectively. For reference, a 0% change corresponds to the dashed-dotted line at $\Delta x = 0$. The black dotted line and dashed line correspond to their identical counterparts in *B*, with a slope of $S_x = \lambda = 16.5 \pm 0.7\%$. (*D*, *Inset*) Time dependence of the linear fitted slopes in boundary positions vs. D plots for x_{Hb} (green) and x_{Eve1} (blue). Error bars are SEs of the fits. For reference, λ, the average length constant of maturation-corrected Bcd gradients of fly lines with Bcd dosages ~1.0 (i.e., fly lines 6–11 in Table S1), is shown in gray. The slope and its fitting error from the linear fit of x_{CF} vs. D in *B* are shown in black. For comparison, the equivalent plot in the concentration representation is shown in Fig. 3*F* (*Inset*) using the conversion $S_c = 1 - \frac{S_x}{\lambda}$ (*SI Materials and Methods*).

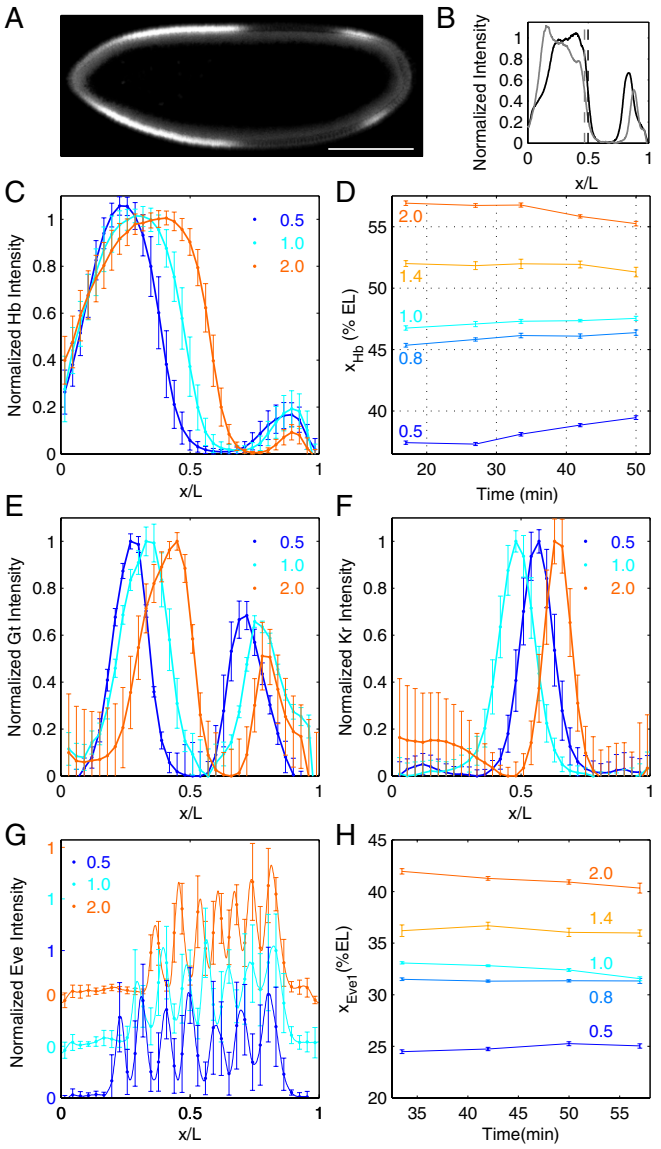

Fig. S7. Response of gap genes to Bcd dosage perturbations. (*A*) Scanning confocal microscopic image of a *Drosophila* embryo of fly line $2X_A$ during nuclear cycle (n.c.) 14, immunostained for Hb. The embryo is imaged in the midsagittal plane, oriented dorsal up and anterior left. (Scale bar: 100 μm.) (*B*) Dorsal (black) and ventral (gray) Hb profiles from the embryo in *A*; normalized fluorescence intensity is a function of fractional egg length *x/L* (*SI Materials and Methods*). Dashed lines indicate the position of the Hb boundary for each profile. (*C*) Average dorsal Hb profiles of embryos fixed 10–24 min into n.c. 14 from fly lines with Bcd dosages of 0.5 (blue; fly line $1X_A$, $n = 67$ embryos), 1.0 (cyan; $2X_A$, $n = 22$ embryos), and 2.0 (orange; $2X_A2III_A$, $n = 37$ embryos). For each line, profiles were binned into 33 equispaced bins along the AP axis. Lines are the mean profile intensity in each bin. Error bars represent the SD of the profile intensity in each bin. (*D*) Mean position of the Hb boundary, x_{Hb}, as a function of time for embryos with Bcd dosages of $D = 0.5$ (dark blue; fly line $1X_A$, $N = \{120, 120, 66, 98, 45, 50\}$ embryos for each time class), D = 0.78 (light blue; $2II_A$, $N = \{79, 95, 45, 65, 28, 9\}$ embryos for each time class), $D = 1.0$ (cyan; fly line $2X_A$, $N = \{73, 65, 52, 105, 44, 16\}$ embryos for each time class), $D = 1.4$ (light orange; fly line $2X_A1II_A$, $N = \{50, 37, 28, 49, 44, 14\}$ embryos for each time class), and $D = 2.0$ (orange; fly line $2X_A2III_A$, $N = \{61, 88, 66, 90, 20, 18\}$ embryos for each time class). Error bars represent the SEM. Time is measured from the beginning of n.c. 14, with each value on the time axis representing the average time in each time class. The equivalent plot of *C* for average dorsal Gt (*E*) and Kr (*F*) profiles in embryos fixed 10–24 min into n.c. 14 is shown. The number of embryos for Bcd dosages of $D = \{0.5, 1.0, 2.0\}$ are $N = \{16, 12, 9\}$ for Gt and $N = \{23, 35, 59\}$ for Kr, respectively. (*G*) Equivalent plot of *C* for average dorsal profiles of Eve in embryos fixed 53–62 min into n.c. 14. The number of embryos for Bcd dosages of $D = \{0.5, 1.0, 2.0\}$ are $N = \{33, 48, 36\}$. Note the arbitrary offset on the *y* axis for visualization purposes. (*H*) Equivalent plot of *D* for the average peak position of Eve–Stripe-1, x_{Eve1}, as a function of time. For Bcd dosages of 0.5, 0.78, 1.0, 1.4, and 2.0, $N = \{45, 81, 33, 16\}$, $\{43, 91, 43, 19\}$, $\{44, 107, 48, 12\}$, $\{10, 39, 15, 9\}$, and $\{9, 42, 36, 9\}$, respectively.

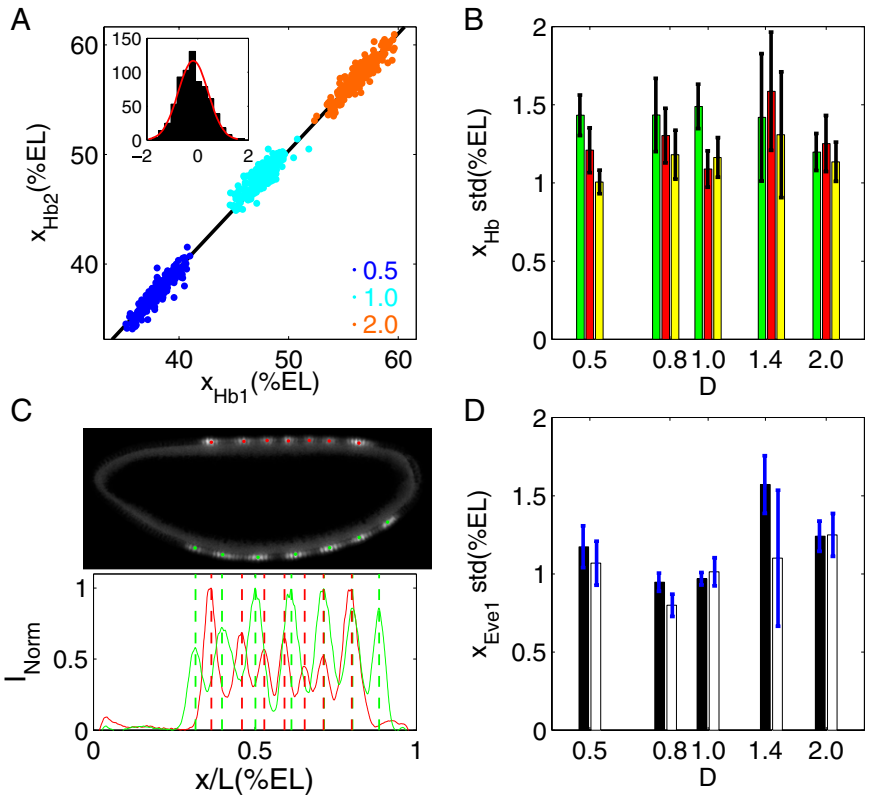

Fig. S8. Measurement error analysis of marker positions. (*A*) Comparison of the Hb boundary position detected with two alternative methods. x_{Hb1} is located at the half-maximal intensity of Hb expression levels, and x_{Hb2} is located where the Hb boundary has its steepest slope. There are a total of 718 embryos from fly lines with Bcd dosage $D = 0.5$ (blue), $D = 1.0$ (cyan), and $D = 2.0$ (orange). (*A*, *Inset*) Histogram of the difference between the two methods (least-square distance of the data points from the diagonal in the main panel). The red curve shows a Gaussian fit with an SD of 0.6%EL. Thus, our estimated error from autodetection of the Hb boundary position is ~0.6%EL. (*B*) Comparison of x_{Hb} *std* (measurement error of Hb boundary positions) under different embryo orientations. Bars represent the SD of x_{Hb} measured with Hb profiles on the ventral side (green) and dorsal side (red). After averaging x_{Hb} from the dorsal and ventral sides for individual embryos, the SD is reduced (yellow bar) for all examined fly lines with Bcd dosage $D = 0.5$–2.0. Error bars are the errors of the SD calculated from bootstrapping. (*C*) Illustration of manual check on auto-detected Eve peaks. The peak positions of Eve stripes were identified by finding seven local maxima in the middle 80% of the embryo after averaging the profile over a spatial region of 3%EL, which is approximately the size of an entire Eve stripe. The auto-detected peak positions [dorsal (red) and ventral (green)] are drawn as dashed lines at their corresponding fractional embryo length *x/L* and as colored dots on the immunostaining image of their corresponding embryo. (*D*) Comparison of x_{Eve1} *std* (measurement error of the peak of the first Eve stripe) with and without classification of embryo age for five fly lines with different Bcd dosage *D*. Bars are the SDs of x_{Eve1} of all embryos (black) and from embryos at the age of 50 ± 3 min into n.c. 14 (white). Error bars are the errors of the SDs calculated from bootstrapping.

Table S1. Fly line library with genetically modified Bcd dosages

Fly line ID no.	Fly line name	Genotype	D	x_{CF} (%EL)
1*	$1II_A$	*yw; egfp-bcd/+; bcd^{E1}*	0.44 ± 0.03	25.1 ± 1.4
2	$1II_C$	*yw; egfp-bcd/+; bcd^{E1}*	0.46 ± 0.04	27.7 ± 1.1
3*,†	$1X_A$	*egfp-bcd/yw; +; bcd^{E1}*	0.52 ± 0.03	26.9 ± 1.3
4*,†	**$2II_A$**	***yw; egfp-bcd; bcd^{E1}***	**0.78 ± 0.08**	**32.0 ± 1.3**
5	**$2II_B$**	***yw; egfp-bcd; bcd^{E1}***	**0.78 ± 0.04**	**32.9 ± 1.0**
6*	$1X_A1II_A$	*egfp-bcd/yw; egfp-bcd/+; bcd^{E1}*	0.93 ± 0.07	33.4 ± 1.1
7	$1II_A1III_A$	*yw; egfp-bcd/+; egfp-bcd,bcd^{E1}*	0.97 ± 0.08	32.9 ± 0.7
8	**$2III_A$**	***yw; +; egfp-bcd,bcd^{E1}***	**0.99 ± 0.17**	**33.6 ± 1.6**
9*,†	**$2X_A$**	***egfp-bcd; +; bcd^{E1}***	**1.00 ± 0.06**	**34.4 ± 1.3**
10	**$2III_B$**	***yw; +; egfp-bcd,bcd^{E1}***	**1.02 ± 0.07**	**32.8 ± 1.2**
11	**$2II_C$**	***yw; egfp-bcd; bcd^{E1}***	**1.09 ± 0.05**	**34.2 ± 1.1**
12*	$1X_A2II_A$	*egfp-bcd/yw; egfp-bcd; bcd^{E1}*	1.25 ± 0.10	37.4 ± 1.6
13*	$2X_A1II_A$	*egfp-bcd; egfp-bcd/CYO; bcd^{E1}*	1.45 ± 0.09	38.2 ± 1.1
14*	$2X_A2II_A$	*egfp-bcd; egfp-bcd; bcd^{E1}*	1.57 ± 0.13	40.0 ± 1.3
15	$2II_A2III_A$	*yw; egfp-bcd; egfp-bcd,bcd^{E1}*	1.78 ± 0.13	41.4 ± 1.5
16*	$2X_A2III_A$	*egfp-bcd; +; egfp-bcd,bcd^{E1}*	2.09 ± 0.14	41.4 ± 1.4
17	$2X_A2III_B$	*egfp-bcd; +; egfp-bcd,bcd^{E1}*	2.12 ± 0.09	40.6 ± 1.0
18*	$2X_A1II_A2III_A$	*egfp-bcd; egfp-bcd/CYO; egfp-bcd,bcd^{E1}*	2.31 ± 0.19	42.9 ± 1.5
19	$2X_A2II_A2III_A$	*egfp-bcd; egfp-bcd; egfp-bcd,bcd^{E1}*	2.34 ± 0.18	45.0 ± 1.4
20*,†	$2X_A2II_c2III_A$	*egfp-bcd; egfp-bcd; egfp-bcd,bcd^{E1}*	2.40 ± 0.17	43.0 ± 1.5
21‡	$1II_A$ BNT	*yw; egfp-bcd/+; bcd^{E1}nos^{BN}tsl^{-}*	0.38 ± 0.06§	19.3 ± 1.2
22‡	$1X_A$ BNT	*egfp-bcd/yw; +; bcd^{E1}nos^{BN}tsl^{-}*	0.44 ± 0.06§	22.5 ± 1.7
23‡	$1X_A$ BT	*egfp-bcd/yw; +; bcd^{E1}tsl^{-}*	0.47 ± 0.07§	23.1 ± 1.0
24‡	$1X_A$ BN	*egfp-bcd/yw; +; bcd^{E1}nos^{BN}*	0.51 ± 0.06§	28.0 ± 1.4
25‡	$2X_A$ BNT	*egfp-bcd; +; bcd^{E1}nos^{BN}tsl^{-}*	0.82 ± 0.10§	32.2 ± 1.3
26‡	$2X_A$ BT	*egfp-bcd; +; bcd^{E1}tsl^{-}*	0.94 ± 0.11§	32.7 ± 1.0
27‡	$2X_A$ BN	*egfp-bcd; +; bcd^{E1}nos^{BN}*	0.99 ± 0.18§	34.4 ± 1.3
28‡	$2X_A1II_A$ BT	*egfp-bcd; egfp-bcd/+; bcd^{E1}tsl^{-}*	1.33 ± 0.20§	36.0 ± 1.6
29‡	$2X_A$ $1II_A$ BN	*egfp-bcd; egfp-bcd/+; bcd^{E1}nos^{BN}*	1.35 ± 0.20§	39.8 ± 1.6

Bcd dosages (D) and CF positions (x_{CF}) are reported as population means with SDs; founder lines are marked in bold. BNT, *bcd-nos-tsl*; BT, *bcd-tsl*; ID, identification.

*Eleven fly lines shown in Fig. 1*F*.

†Egg-hatching rates of fly lines 3, 4, 9, and 20 are 48%, 89%, 91%, and 67%, respectively. We were unable to generate fly strains that had Bcd dosages smaller than 0.44 or larger than 2.8. We believe these values correspond to the boundaries of viability. For all other generated fly lines, we obtained viable offspring, with hatching rates dropping for dosages close to these boundaries, consistent with earlier reports (1).

‡Nine maternal mutant fly lines shown in Fig. 4*A*. The only fly lines with maternal mutant backgrounds that we were able to generate are the ones shown here.

§The *nos* or *tsl* mutations slightly affect the nuclear Bcd compared with the same *egfp-bcd* insertions in a WT background. Tsl^{-} reduces Bcd dosage by about 10% (D of fly lines 23 vs. 3, 26 vs. 9, and 28 vs. 13) and the double mutation *tsl*/*nos* reduces the Bcd dosage by about 15% (D of fly lines 22 vs. 3, 21 vs. 1, and 25 vs. 9). The *nos* background alone does not appear to affect the Bcd dosage (D of fly lines 24 vs. 3, 27 vs. 9, and 29 vs.13). These Bcd dosage differences with respect to WT are very close to our measurement error, and the mutant embryo sample sizes are much smaller than those for the Bcd-GFP fly lines in WT background. Therefore, it is uncertain whether the observed differences of Bcd dosages are statistically significant for our measurements.

1. Namba R, Pazdera TM, Cerrone RL, Minden JS (1997) Drosophila embryonic pattern repair: How embryos respond to bicoid dosage alteration. *Development* 124(7):1393–1403.